Computer-aided Estimation of Plastic Properties Using Instrumented Indentation Tests

Chen Ta-Te

February 2022

Computer-aided Estimation of Plastic Properties Using Instrumented Indentation Tests

Chen Ta-Te
Doctoral Program in Materials Science and Engineering

Submitted to the Graduate School of
Pure and Applied Sciences
in Partial Fulfillment of the Requirements
for the Degree of Doctor of Philosophy in
Engineering

at the
University of Tsukuba

Abstract

COMPUTER-AIDED ESTIMATION OF PLASTIC PROPERTIES USING INSTRUMENTED INDENTATION TESTS

Chen Ta-Te

For structure materials, tensile and compression tests are standard methods for characterizing mechanical properties based on the stress-strain curve because of the simple stress state. However, these tests require considerable effort and time for specimen preparation and conducting tests under various conditions. Instrumented indentation tests are an efficient approach for evaluating mechanical properties, such as effective elastic stiffness and hardness, that require less effort for specimen preparation and provide multiple results from a sample. Instrumented indentation's non-destructive, high throughput, and multi-scale nature makes it widely employed in material science and engineering.

In this thesis, the estimation method of plastic properties using instrumented indentation has been proposed. The suitable constitutive model has been used to reproduce the deformation behaviors of alloys, and both experimental and numerical approaches determined the corresponding material constants. From the experimental results of instrumented indentation, the load – depth curves (i.e., the *P–h* curve), pile-up topography, rate-dependency, and the curvature difference between two indentations at neighboring positions were utilized to characterize the material properties. Numerical simulations estimated the response of material constants on instrumented indentation, and the material parameters were determined by gradient descent or data-driven method.

The proposed method was validated for application to aluminum alloys and stainless steel. Firstly, the estimation results using pile-up height and loading curvature of the $P-h$ curve show good agreement with experimental tensile results and existing approaches. The neighboring indentation test was also used to determine the material constants, which offers more accurate estimation results than only considering the single $P-h$ curve and pile-up height. But the linear hardening behavior of stainless steel cannot be represented by a simple power-law hardening model; a new estimation method with the modified constitutive model was proposed to improve the accuracy of the estimation results.

To further extend the application of the proposed estimation method, the instrumented indentation results with different loading rates were used to determine the material constant of a modified rate-dependent constitutive model. Finite element simulations using estimated mechanical properties were compared with the corresponding experiments in compression tests at the same temperature to validate the estimated material responses. The constitutive model and determined material constants can reproduce the strain-rate-dependent material behavior under various loading speeds in instrumented indentation tests; however, the load level of computational simulations is lower than those of the experiments in the compression tests. These results indicated that the local mechanical responses evaluated in the instrumented indentation tests were not consistent with the bulk responses in the compression tests at high temperatures. The scale effect remarkably appears at high temperatures.

In summary, a new estimation method of plastic properties using instrumented indentation tests has been proposed. These methods can be widely applied to various alloys and provide an efficient, high-throughput way for material database creation that is necessary to accelerate material research and development. This study also shows the probability of characterizing the high-temperature plasticity of alloys using instrumented indentation, but further study is needed to solve the complex deformation mechanism and tremendous scale effect at high temperature.

Acknowledgments

Feb. 2022.

Chen Ta-Te

First and foremost, I would like to give my sincere gratitude to my supervisor, Prof. Ikumu Watanabe, who provided this precise opportunity and tremendous support to my doctoral research. His board and profound knowledge, great experience, enthusiasm, motivation, and careful study show me the way an outstanding researcher should be. I sincerely appreciate his patience and kindly instrument for all my research. Thank Prof. Akinobu Shibata, Prof. Hee Young Kim, and Prof. Koichi Tsuchiya for being on my dissertation committee and providing insightful comments and suggestions.

I wish to acknowledge Prof. Tatsuya Funazuka for providing aluminum alloy samples and assistance with the experiment, Prof. Hideyuki Murakami, and Dr. Daisuke Araki for the technical support and experiment facilities. I would also like to give my gratitude to all members of the High Strength Materials Group in NIMS, Prof. Takahito Ohmura, Prof. Masato Wakeda, Prof. De-hai Ping, Dr. Kenta Goto, Dr. Yanxu Wang, Dr. Hongxing Li, and Ms. Eri Nakagawa for their professional advice, countless help, and providing experiment environment. Thanks, Ms. Yuki Yamamoto, Dr. Sachiko Taniguchi, Ms. Midori KUbota, and Ms. Rie Iguchi, for all the help and support in my study and life in Japan. In the last three years, I have been so happy with all my fellow lab-mates, Zhengzhong Sun, Dayuan Liu, Jiaxin Zhou, Dr. Viola Paul, Yizen Cao, Weikang Song Xiaoyang Zheng, and Tianwen Tan, for all your accompany and friendship. I would also like to thank Prof. Naito Masanobu, Dr. Pruksawan Sirawit, Dr. Hsing-Ying Tsai, Dr. Wei-Hsun Hu, and Dr. Siqian Wang in the Data-driven Polymer Design group for the interdisciplinary discussion and cooperation.

Last but not least, I gratefully appreciate my parents for their love and support. It would be impossible to finish my doctoral study without their understanding and encouragement. Thanks to all my friends for all the fun and challenging days in my life.

Contents

List of Tables

List of Figures

Chapter 1

Introduction

1.1 Background

Material tests are essential to evaluate material properties, and efficient test methods are required to establish a material database for the computer-aided framework to accelerate material research and development. In structural materials, tensile and compression tests are standard methods for evaluating mechanical properties such as elastic stiffness, yield strength, and work-hardening. The stress-strain curve is measured as raw data. Although a simple stress state can be assumed in these material tests, considerable effort is required to prepare specimens and conduct the tests. In this context, the hardness test, in which the resistance to the imposed plastic deformation is measured on the surface, has been utilized as an efficient approach to estimate the mechanical properties in the industry. It can also be used to evaluate small-scale mechanical properties by controlling a small load; that is, the mechanical properties of a heterogeneous microstructure can be assessed [2),3),5)]. Using this technology, a high-throughput evaluation of macroscopic mechanical properties has been conducted to characterize the microscopic heterogeneity [6),7)] and obtain massive material data[8)].

The instrumented indentation test, the depth-sensing indentation test, extends the hardness test[9)]. The applied load and penetration depth is measured in the instrumented indenta-

tion test. Based on the resulting relationship between load P and depth h (i.e. the P–h curve) the elastic stiffness and hardness can be estimated [10]. Compared with the uniaxial stress state in tensile or compression tests, the instrumented indentation test produces an inhomogeneous stress state. So it isn't easy to directly get the stress-strain curves corresponding to the uniaxial tensile test from instrumented indentation test. Existing estimation methods and their limits will be discussed in the section1.3.2.

This chapter will introduce the basic theory of metal plasticity, followed by strain-rate-dependent plasticity. After that, the estimation method of elastic modulus and hardness from instrumented indentation test will be discussed. And following with the introduction of existing approaches to estimate the plastic properties and applications in the material science and engineering field. Finally, the Purpose and objectives will be introduced.

1.2 Mechanical properties of alloys

For a typical ductile metal, the common stress σ and strain ε curve of the tensile test are shown in **Fig. 1.1**. The specimen was first subjected to axial stress from 0 to σ_0, then unloaded back to an unstressed state and subsequently reloaded to higher stress σ_1. The stress-strain curve follows the path $ABCDEF$. The first stage of the tensile test, AB, shows the linear elastic behavior of metals after the stress is greater than the initial yield point B, the plastic deformation starts, and the slope of the curve changes immediately. When stress unloading at C, an elastic relaxation like AB can be observed, and the difference between A and D is the plastic strain ε_p caused by the plastic deformation from B to C. When reloading from D to E, the linear elastic behavior can be observed without being affected by previous plastic deformation. Beyond E, the plastic deformation starts again until the final stress F. It is worth noting that the difference between unloading (CD) and reloading (DE) curves in the actual tensile test will be much smaller than **Fig. 1.1**.

Some important phenomenological properties can be identified in the above-described tensile test.

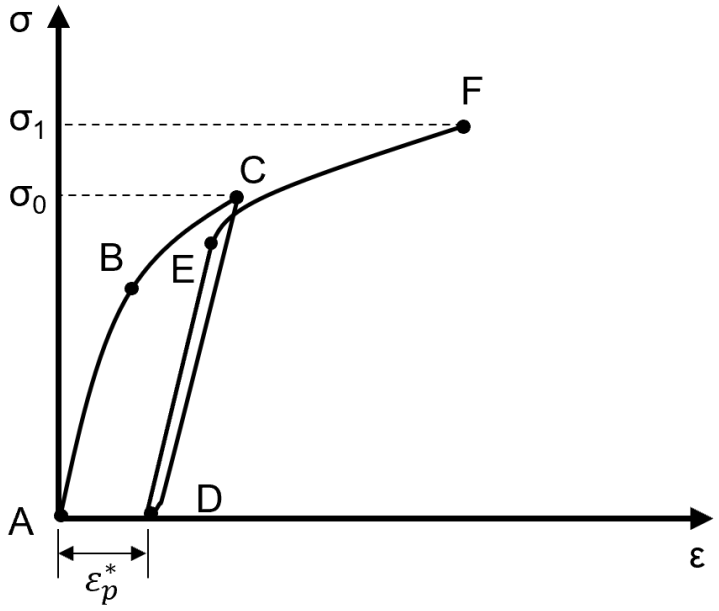

Fig. 1.1 The schematic diagram of the typical stress-strain curve of ductile metals from the uniaxial tensile test.

1. Like *AB* and *DE*, the range of stresses that the material behavior can be considered purely elastic, called elastic domain.

2. When the stress is higher than the yield stress, plastic yielding (or plastic flow) with plastic strain occurs.

3. After the plastic deformation, the yield stress increase, the difference between *B* and *E* is called hardening.

Empirical stress-strain equations

In the theoretical treatment of the plasticity problem, it is beneficial to represent the true stress-strain curve by a suitable empirical equation with material constants that can be fitted to the experimental results. For example, the most straightforward power-law empirical equation was proposed by Hollomon [11]:

$$\sigma = C\varepsilon_p^n \tag{1.1}$$

where C is a plastic coefficient, and n is the strain hardening exponent. The value of n usually is less than 0.5. In this equation, the initial yield stress is not considered. The Ludwik [12] equation is similar but with the initial yield stress term Y as follows.

$$\sigma = Y(1 + m\varepsilon_p^n) \tag{1.2}$$

where m is constant, there are also have some well-used empirical equations with different formats, like the Swift equation and Voce equation. The Swift equation is

$$\sigma = C(m + \varepsilon_p)^n \tag{1.3}$$

And the Voce equation is

$$\sigma = C(1 - me^{-n\varepsilon_p}) \tag{1.4}$$

The empirical stress-strain curves can be represented by those equations, like the examples in **Fig. 1.2**, and the material constants can be fitted by the experimental results. The basic theory of metal plasticity and the constitutive model used in this study will be discussed in the section2.2.

1.3 Instrumented indentation test

From the industrial revolution, many raw materials, like iron, copper, wood, rubber, etc., are needed for mass production in various fields like agriculture, engineering, industry, etc. The tremendous demand for steel made the mining industry grow fast, and a simple, fast, and efficient material quality test method became necessary. In 1812, mineralogist Friedrich Mohs [13] first developed the method to characterize the hardness of minerals by scratching the sample, but it could not give the exact value. The hardness testing by indentation was first reported by William Wade [14] in 1856, a specified load was applied to a pyramid

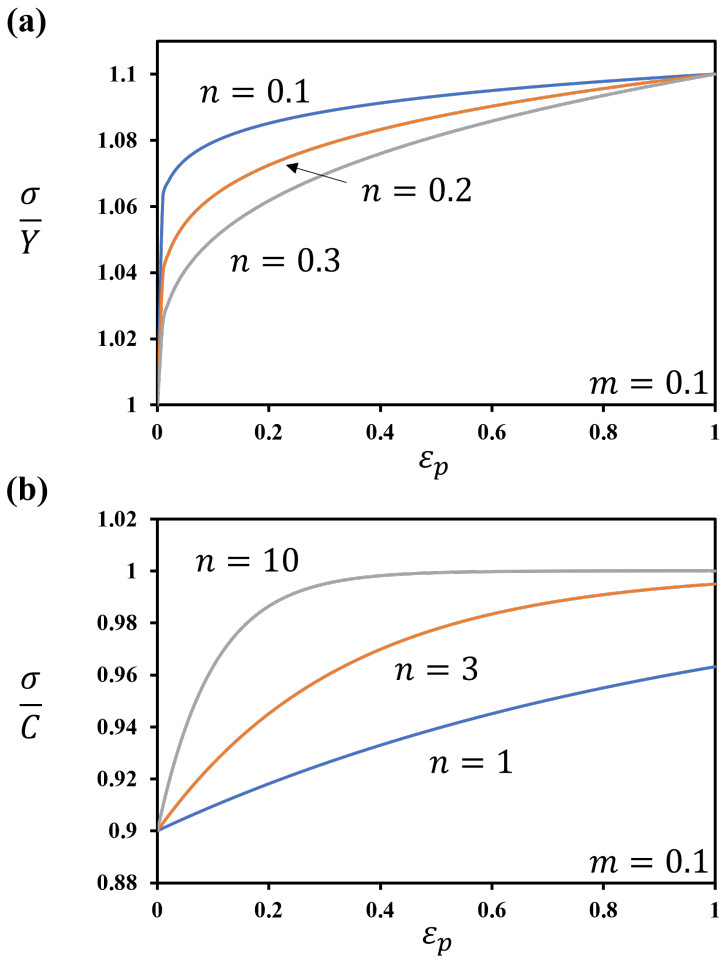

Fig. 1.2 The empirical stress-strain curve from (a) Ludwik equation (b) Voce equation.

indenter, and the hardness was calculated from the size of the remained impression mark. The indentation test had been widely used in industry due to the simplicity in the beginning of twentieth-century and several indentation method had been established, like Brinell [15], Meyer [16], Vickers [17], Rockwell [12], Knoop [18], etc., in different scale and become a standard method to estimate the mechanical properties[19),20),21)]. Thanks to the recent development of computer technology and sophisticated instruments, the indentation test extend its application to micro and nano-scale, making it very powerful to characterize the multi-scale mechanical properties at various conditions. The scientific study of the mechanism of indentation tests was discussed by Hill [22], and Tabor [23] in the 1950s, which combined the theoretical research and experimental approach to provide the deeper physical insight for the understanding of the nature of deformation during indentation tests. I want to explain some fundamental theories and the estimation method of elastic modulus and hardness using the indentation test.

1.3.1 Estimation of elastic modulus and hardness

In instrumented indentation test, the displacement h and load P are continuously monitored with high accuracy and acquiring rate, the typical load-displacement curve (i.e. the P–h curve) is schematically shown in **Fig. 1.3**

During the instrumented indentation test, the indenter will be pushed into the sample surface until a predetermined load P_{max} or depth h_{max}, depending on the control mode, is reached. After holding times at peak load (or depth) to eliminate the rate-dependent effect, the indenter will withdraw from the sample, and the residual penetration depth h_f is measured. From the unloading curve, the slope of the upper part is called the elastic contact stiffness:

$$S = \frac{dP}{dh} \tag{1.5}$$

In the instrumented indentation, the hardness of the material, which means the materials' resistance to plastic flow, is defined as:

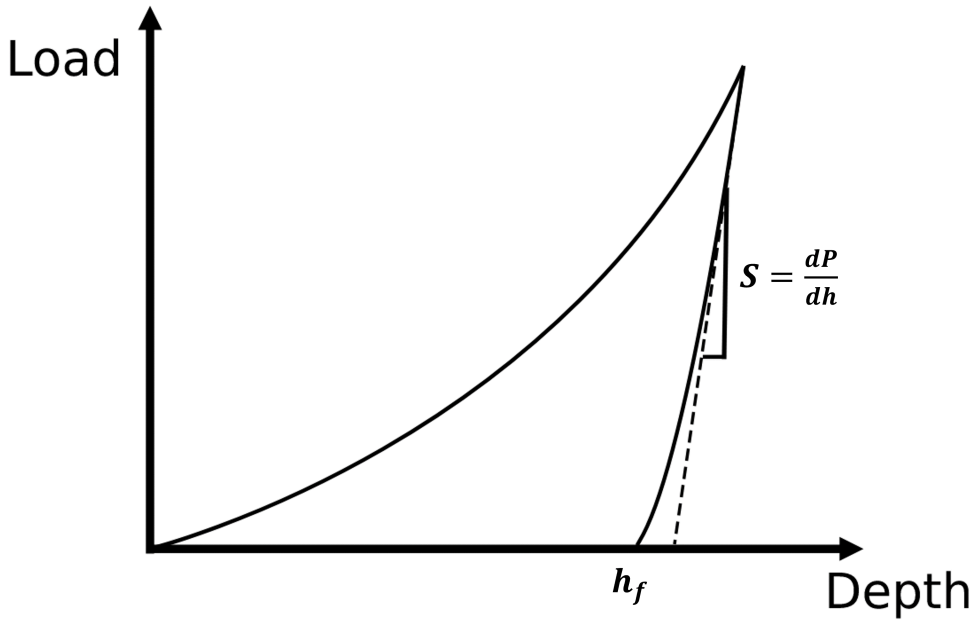

Fig. 1.3 The typical load – depth curve of instrumented indentation.

$$H = P/A_p \tag{1.6}$$

where A_p is the projected area of the indenter contact sample, in micro-and nano-scale, the indented area becomes too small to observe using common optical microscopy, and it becomes a problem. However, a helpful method has been developed to calculate the indented area from the *P–h* curve.

Oliver-Pharr analysis method

Oliver and Pharr proposed a method in the 1990s to calculate H and elastic modulus E from the *P–h* curve without any need to measure the deform area with a microscope[10] directly. They assumed the unloading part of the *P–h* curve is purely elastic and follows the power-law relation derived from the elastic contact theory:

$$P = \beta\left(h - h_f\right)^m \tag{1.7}$$

where β and m are empirically determined fitting constants. By combining Eq. (1.5) and (1.7), the contact stiffness S at maximum depth h_{max} can be derived as:

$$S = \left(\frac{dP}{dh}\right)_{h=h_{max}} = \beta m \left(h_{max} - h_f\right)^{m-1} \tag{1.8}$$

The next step is to determine the actual contact depth h_c which is shown in fig. For pure elastic contact and assuming the pile-up is negligible, the amount of sink-in h_s is given by:

$$h_s = \varepsilon\left(\frac{P_{max}}{S}\right) \tag{1.9}$$

where ε is a constant depending on the geometry of the indenter [24]. For Berkovich and cube-corner indenter, the $\varepsilon = 0.75$. The geometry of a Berkovich indenter shown in **Fig. 1.4**

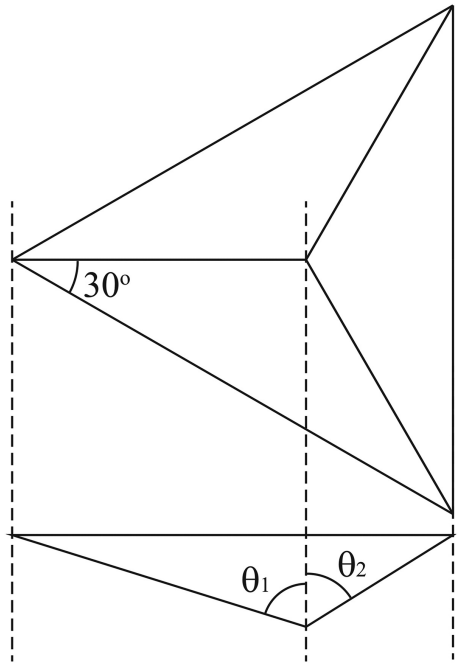

Fig. 1.4 Geometry of a triangular pyramidal indenter.

The contact depth h_c then can be estimated by:

$$h_c = h_{max} - h_s = h_{max} - \varepsilon P_{max}/S \tag{1.10}$$

For an ideal Berkovich indenter, the projected area can be calculated as:

$$A_p = 3\sqrt{3}\tan^2(\alpha/2)\,h_c^2 = 24.56h_c^2 \tag{1.11}$$

where $\alpha = 130.6°$. By combining with the Eq. (1.10) and calculated elastic stiffness S, the hardness $H = P_{max}/A_p$ can be calculated.

But in the real world, the Berkovich indenter always with some blunted or defects from manufacturing or testing, which caused a potential error of estimated results. Oliver and Pharr provided a quite useful method to calibrate the indenter area by introducing area function $A_p = f(h_c)$ as:

$$A_p = f(h_c) = 24.56h_c^2 + C_1h_c^1 + C_2h_c^{1/2} + C_3h_c^{1/4} + ... \tag{1.12}$$

The first term of the polynomial fit corresponds to the ideal Berkovich indenter. The remaining terms can be fitted by using a standard sample, which the elastic modulus is known, like fused quartz.

The elastic modulus can be calculated by:

$$S = \frac{2}{B\sqrt{\pi}}E_r\sqrt{A_p} \tag{1.13}$$

where B is a geometrical constant of indenter [24], for Berkovich indenter the $B = 1.034$[25], and E_r is the reduced elastic modulus defined as:

$$\frac{1}{E_r} = \frac{1-\nu^2}{E} + \frac{1-\nu_i^2}{E_i} \tag{1.14}$$

where E and ν are the elastic modulus and Poisson's ratio of the sample and E_i and ν_i are the elastic modulus and Poisson's ratio of indenter. The reduced elastic moules E_r is contributed by elastic deformation of both sample and indenter during indentation, the $E_i = 1140$GPa and $\nu_i = 0.07$ for common used diamond indenter.

Hertz contact theory

H. Hertz [26] is the first to study the contact theory between two elastic samples, which is very useful for quantifying the contact area and stress state between a rigid spherical indenter

and the elastic sample surface. The radius of the contact area of the spherical indenter could be defined as follows:

$$r_c^3 = \frac{3}{4}\frac{PR_i}{E^*} \tag{1.15}$$

where P is the load, R_i is the radius of the tip, and E^* is the reduced modulus. The E_r can be described as follows:

The relationship between load P and penetration depth h during pure elastic deformation can be described as:

$$P = \frac{4}{3}E^*\sqrt{R_i}h^{\frac{3}{2}} \tag{1.16}$$

Hertz's contact theory is very useful to identify the elastic-plastic transition by fitting the load-displacement curves of the indentation test.

Pile-up and sink-in phenomenon

One of the critical issues in instrumented indentation is the pile-up and sink-in phenomenon. The schematic diagram of the pile-up and sink-in phenomenon is shown in **Fig. 1.5**. When the indenter is pressed into the sample surface, the materials around the indenter will be drawn down or raised upward. Because of the pile-up and sink-in phenomenon, the measured contact depth h_c may not be accurate, since the depth is measured from the original surface of the sample h. The pile-up behavior was investigated for various materials [27),28),25)]. It depends on the elastoplastic properties, particularly the strain hardening exponent.

1.3.2 Estimation of plastic properties

In the previous section, we discuss the estimation method of elastic modulus and hardness using the indentation test. Here we will talk about estimating plastic properties using the indentation test.

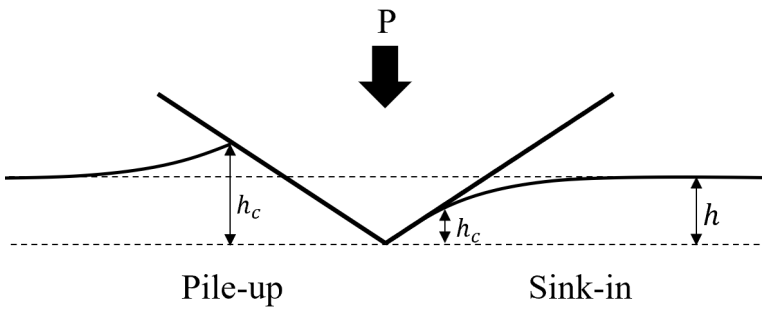

Fig. 1.5 Schematic diagram of pile-up and sink-in phenomenon.

Existing approaches

Various estimation approaches for the stress-strain relationship corresponding to the tensile test have been proposed based on instrumented indentation tests. In this field, it is recognized that a unique stress-strain relationship cannot be estimated from the *P–h* curve of a single indentation using a standard sharp indenter [29),30),31)]. In this context, a dual-indenter approach spherical indenter approach was established. The dual-indenter approach [32),33),34)] using two sharp indenters with different apex angles enables us to determine a unique set of material parameters in a simple constitutive model. But this method is found to be sensitive to an experimental error during the change of indenters with different geometry[35)], and it costs a lot of time to calibrate a new indenter. The spherical indentation approach [36),37),38),39)] is based on the nonlinear relationship between the indentation depth and cross-sectional area of the indentation, which will be hugely affected by the pile-up and sink-in phenomenon.

Those approaches focus only on the *P–h* curves. But in this thesis, the topography of the pile-up and the interaction between two neighboring indentations were considered to determine the plastic properties.

1.3.3 Applications of instrumented indentation test

The non-destructive, multi-scale, high-throughput nature of instrumented indentation tests attracts lots of attention to applying this technique to different materials and applica-

tions. Some recent studies utilize instrumented indentation to characterize desired mechanical properties. For example, the microscopic heterogeneity of materials is one of the most critical issues in recent years[6),5)]. Ruzic et al. [2)] characterize the effect of Mo segregation and distribution in Ti-Mo alloy on mechanical properties using nanoindentation. They found that the Mo segregation had a significant impact on the mechanical properties as well as the distribution of the ω_{iso} phase within the grains. The high amount of ω_{iso}-precipitates in the Mo-lean regions caused the higher hardness and elastic modules value while the Mo-rich region without ω_{iso}-precipitates exhibited the lowest values shown in **Fig. 1.6** .

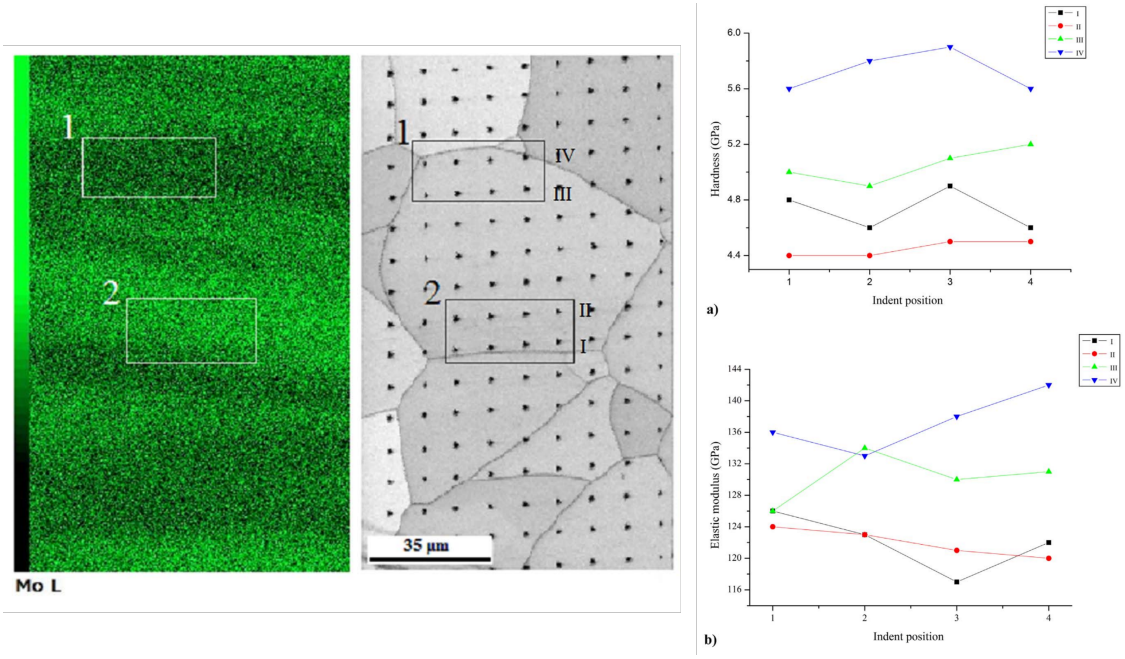

Fig. 1.6 The EDS and IQ image of the sample and the indents made in regions with (1) higher and (2) lower Mo contents within a single grain. [2)]

The mechanical behavior of multilayer steel structures fabricated via wire and arc additive manufacturing (WAAM) has been investigated by Watanabe et al. [3)] from a multiscale perspective. The multimaterial WAAM approach can control the heterogeneous structure and improve its mechanical properties by optimizing the process parameters. The microscale heterogeneous mechanical properties of the duplex-phase multilayer steel structures were characterized through micro-indentation in **Fig. 1.7**. Those results were then used to char-

acterize the macro-scale deformation behavior of WAAM samples using the finite element model.

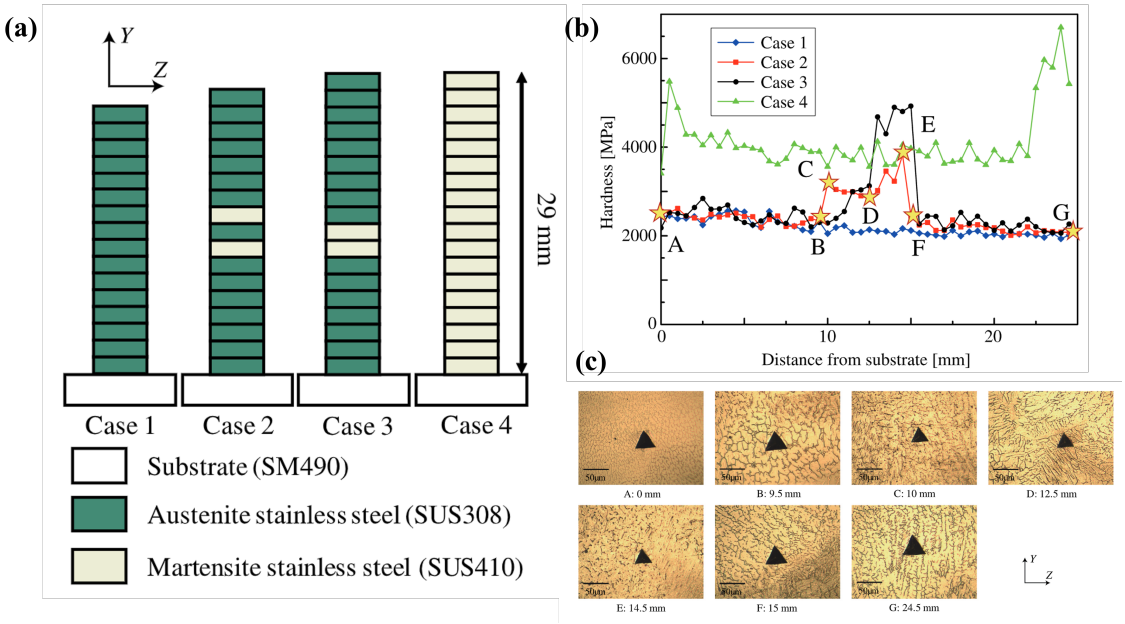

Fig. 1.7 (a) Multilayer steel structures fabricated via WAAM. (b) Indentation hardness distributions of multilayer steel structures. (c) Microstructure around indentation areas in Case 2. [3)]

The instrumented indentation is also used to characterize the complex deformation mechanisms [40)]. Man et al. [41),42)] studied the effect of boundary or interface on activation and interaction of stress-induced martensitic transformation using nanoindentation. They found that the P/h versus h plots show good potential to characterize the multi-deformation mechanism during indentation, and the results indicated that martensitic transformation is significantly retarded by boundaries. Retardation presumably depends on the character of boundaries due to a constraint against volume expansion of the transformation from γ to α' .

Those studies focus on the deformation behavior at room temperature. Still, instrumented indentation tests at elevated temperatures have also attracted considerable attention to characterizing the temperature dependency of mechanical properties, which has the potential for efficiently obtaining material databases for the research and development of heat-

resistant materials. In this context, Chen et al. [7] applied nanoscopic instrumented indentation tests at elevated temperatures to the high-throughput screening of alloy compositions in AlFeCrNiMn high-entropy alloy systems. In particular, high-temperature nanoindentation equipment has been developed in recent years. Suzuki and Ohmura [43] first reported high-temperature nanoindentation measurements up to 600°C on silicon samples. Ruzic et al. [44),4] extended the maximum temperature to 800 °C under an inert atmosphere to investigate the temperature-dependent deformation behavior of γ and γ' single-phase nickel-based superalloys. The elastic modulus and hardness of the γ phase in **Fig. 1.8** decrease as the temperature increases. In contrast, the γ' phase demonstrates thermal stability up to 573 K, indicating the γ' phase domination for the high-temperature property in the dual-phase alloy.

1.4 Purpose and objectives

Instrumented indentation test is an efficient way to characterize the multi-scale mechanical properties of materials at different conditions, like effective elastic stiffness and hardness. But standard stress-strain curves corresponding to tensile test cannot be directly determined from the indentation test results due to the non-uniform deformation behavior. Some estimation methods have been proposed, but some issues like accuracy problems or experimental limits still need to be solved.

This thesis proposed a new estimation method of plastic properties using instrumented indentation test, and the details will be introduced in the following chapters.

In Chapter 2, the suitable experimental parameters for inverse estimation will be discussed. A new test method was proposed to estimate the plastic properties utilizing the interaction between two indentations at neighboring positions called the neighboring indentation method. Two different solution methods were used to determine the suitable material constants of constitutive models from experimental results.

In Chapter 3, the proposed estimation methods were validated in application on aluminum alloys and stainless steel by different approaches. From the pile-up topography and neighboring indentation test, the estimated material constants were validated by the experi-

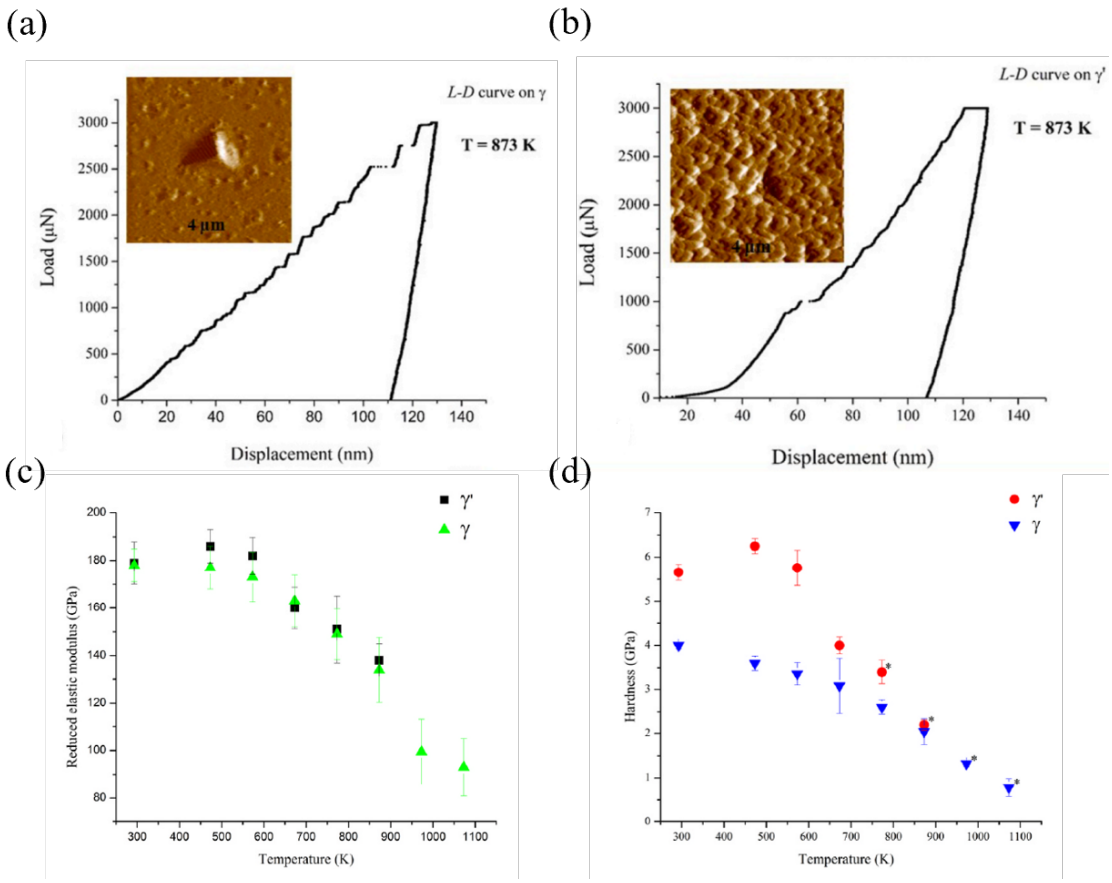

Fig. 1.8 The Load – displacement curves with SPM images on (a) γ and (b) γ' sample at 873 K. The reduced elastic modulus (c) and hardness (d) at different temperatures of the γ and γ'. [4)]

mental tensile test.

In Chapter 4, the proposed estimation methods were extended to characterize the strain-rate-dependent deformation behavior of alloys. A rate-dependent constitutive model was established, and the material constants were determined by the indentation results with different loading rates. This approach was validated on the application of aluminum alloy at high temperatures.

In Chapter 5, the conclusion and future plan of the proposed estimation method will be discussed.

Chapter 2

Estimation method of plastic properties using instrumented indentation

2.1 Introduction

In this Chapter, the basic theory of metal plasticity and the constitutive models used in this study were introduced. The suitable experimental parameters and indentation conditions for inverse estimation were examined by numerical simulations. Two different solution methods were used to determine the suitable material constants of constitutive models from experimental results.

2.2 Constitutive model

2.2.1 Basic theory of metal plasticity

The object of the mathematical theory of plasticity is to provide continuum constitutive models capable of describing (qualitatively and quantitatively) with sufficient accuracy the phenomenological behaviour of materials that possess the characteristics discussed in section 1.2.

In the beginning, the stress – strain curve in **Fig. 1.1** will be simplified to a ideal form

in **Fig. 2.1** where the difference between the CD and DE will be ignored. Following the loading sequence discussed before, when the specimen is reloaded between D and E, the equivalent stress – strain relationship can be expressed as:

$$\sigma^* = E^*(\varepsilon^* - \varepsilon_p^*), \tag{2.1}$$

where σ^*, ε^*, ε_p^*, and E^* is the von Mises stress norm, equivalent strain, equivalent plastic strain, and equivalent Young's modulus of the sample and the difference between total strain and plastic strain $\varepsilon^* - \varepsilon_p^*$ is fully reversible, which will be further discussed in the following.

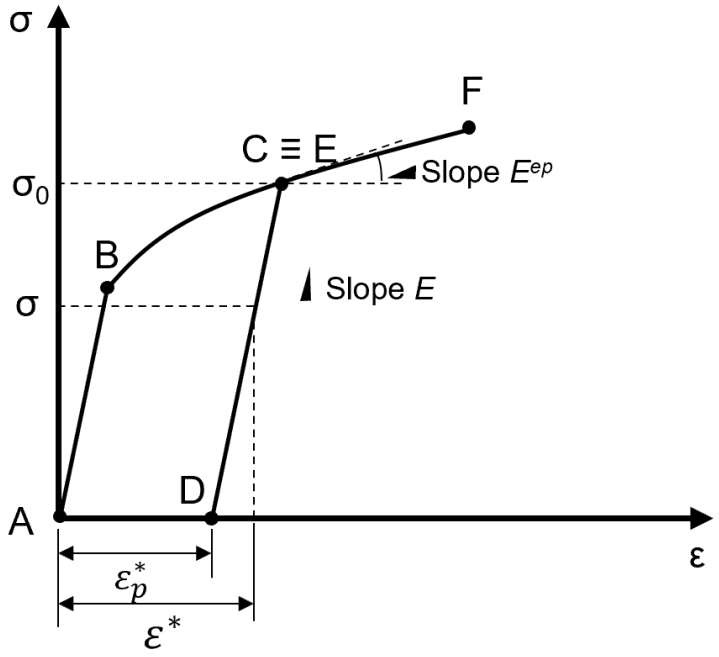

Fig. 2.1 The idealized stress – strain curve from uniaxial tensile test.

Elasto-plastic decomposition

One of the chief hypothesis underlying the small strain theory of plasticity is the decomposition of the equivalent total strain, ε^*, into the sum of an equivalent elastic strain ε_e^* and equivalent plastic strain ε_p^*,

$$\varepsilon^* = \varepsilon_e^* + \varepsilon_p^*, \tag{2.2}$$

where the equivalent elastic strain has been defined as

$$\varepsilon_e^* = \varepsilon^* - \varepsilon_p^*. \tag{2.3}$$

The elastic uniaxial constitutive law

Following the above definition of elastic strain, the elastic constitutive law can be expressed as

$$\sigma^* = E^* \varepsilon_e^* \tag{2.4}$$

which shows the stress – strain relationship in elastic state. The next step is to discuss the plastic part, yield criterion and plastic flow rule.

The yield function and the yield criterion

To define the elastic domain, a yield function Φ is needed

$$\Phi(\sigma^*, \sigma_y) = \sigma^* - \sigma_y, \tag{2.5}$$

and the elastic domain can be defined as the set

$$\mathcal{E} = \{\sigma^* | \Phi(\sigma^*, \sigma_y) < 0\}, \tag{2.6}$$

or it can also be define as

$$\sigma^* < \sigma_y \tag{2.7}$$

It should be noted that the no stress level is allowed above the current yield stress. So, any stress must satisfy the the following condition

$$\Phi(\sigma^*, \sigma_y) \leq 0. \tag{2.8}$$

and the yield criterion can be expressed by

$$\text{If} \quad \Phi(\sigma^*, \sigma_y) < 0 \Longrightarrow \dot{\varepsilon}^p = 0, \tag{2.9}$$

$$\text{If} \quad \Phi(\sigma^*, \sigma_y) = 0 \Longrightarrow \begin{cases} \dot{\varepsilon}^p = 0 & \text{for elastic unloading,} \\ \dot{\varepsilon}^p \neq 0 & \text{for plastic loading.} \end{cases} \tag{2.10}$$

von Mises yield criteria

The most common yield criterion to describe the plastic yielding in metals was purposed by von Mises[45], plastic yielding begin when the J_2 stress deviator invariant reaches a critical value. The concept of stress invariant was purposed by Nayak and Zienkiewicz[46]

$$J_2 = R(\alpha) \tag{2.11}$$

where R is the critical value, which is a function of hardening internal variable α and $J_2 = J_2(s)$ is the invariant of the stress deviator, s, defined by

$$J_2 \equiv -I_2(\boldsymbol{s}) = \frac{1}{2} tr[\boldsymbol{s}^2] = \frac{1}{2}\boldsymbol{s} : \boldsymbol{s} = \frac{1}{2}\|\boldsymbol{s}\|^2. \tag{2.12}$$

the stress deviator is given by

$$\boldsymbol{s} \equiv \boldsymbol{\sigma} - \frac{1}{3}(tr\boldsymbol{\sigma})\boldsymbol{I}. \tag{2.13}$$

where $\boldsymbol{I}$ is the identity tensor.From the definition of the von Mises criterion, the plastic yielding will only be affected by the deviatoric stress and that means the von Mises criterion is pressure-insensitive and isotropic.

An alternative definition of the von Mises yield function can be expressed as

$$\Phi(\boldsymbol{\sigma}) = q(\boldsymbol{\sigma}) - \sigma_y \tag{2.14}$$

where $\sigma_y \equiv \sqrt{3R}$ is the uniaxial yield stress and

$$q(\boldsymbol{\sigma}) \equiv \sqrt{3J_2(\boldsymbol{s}(\boldsymbol{\sigma}))} \tag{2.15}$$

is termed the von Mises effective or equivalent stress. The uniaxial and shear yield stresses fir the von Mises criterion are related by

$$\sigma_y = \sqrt{3}\tau_y \tag{2.16}$$

Plastic flow rules

Equation (2.9) and (2.10) have defined plastic yield condition. Under plastic deformation, the plastic strain rate can be represented as

$$\dot{\varepsilon}^p = \dot{\gamma} sign[\sigma] \tag{2.17}$$

where the scalar $\dot{\gamma}$ is termed the plastic multiplier and is non-negative, and satisfies the complementarity condition

$$\Phi\dot{\gamma} = 0. \tag{2.18}$$

Those constitutive equations mean that when the stress state is in elastic domain,

$$\Phi < 0 \Longrightarrow \dot{\gamma} = 0 \Longrightarrow \dot{\varepsilon}^p = 0, \tag{2.19}$$

and the plastic deformation occur when the yield criterion is fulfilled

$$\sigma^* = \sigma_y \Longrightarrow \Phi = 0 \Longrightarrow \dot{\gamma} \geq 0. \tag{2.20}$$

So the constraints of the elastic-plastic model will be

$$\Phi \leq 0 \quad \dot{\gamma} \geq 0 \quad \dot{\gamma}\Phi = 0. \tag{2.21}$$

The Prandtl-Reuss plasticity law is the flow rule obtained by taking the von Mises yield function as the flow potential. The corresponding flow vector is given by

$$\boldsymbol{N} \equiv \frac{\partial \Phi}{\partial \boldsymbol{\sigma}} = \frac{\partial}{\partial \sigma}\left[\sqrt{3J_2(\boldsymbol{s})}\right] = \sqrt{\frac{3}{2}}\frac{\boldsymbol{s}}{||\boldsymbol{s}||}, \tag{2.22}$$

and the flow rule results in

$$\dot{\varepsilon}^p = \dot{\gamma}\sqrt{\frac{3}{2}}\frac{\boldsymbol{s}}{||\boldsymbol{s}||} \tag{2.23}$$

In the Prandtl-Reuss law, the N and σ are coaxial and Due to the pressure-insensitivity of the von Mises yield function, the plastic flow vector is deviatoric. The Prandtl-Reuss rule is usually employed in conjunction with the von Mises criterion and the resulting plasticity model is referred to as the von Mises associative model or, simply, the von Mises model.

Hardening laws

The Hardening laws represent the evolution of yield stress with plastic strain in one-dimensional problem discussed before. In two- and three-dimensional problem, the hardening is represented by changing in the hardening thermodynamical force, $\boldsymbol{A}$, during plastic yielding. These changes may, in general, affect the size, shape and orientation of the yield surface, defined by $\Phi(\boldsymbol{\sigma}, \boldsymbol{A})$ .It will be said to be perfect plastic model if there is no hardening behavior, which means the yield surface remain fixed during deformation and the elasto-plastic modules $E^{ep} = 0$. If the yield surface expand uniformly during deformation, it called isotropic hardening which shows in **Fig. 2.2**.

In metal plasticity, the density of dislocations usually be considered as the hardening internal variable that caused the isotropic resistance to plastic flow. To describe the isotropic hardening behavior, there are two popular approaches, strain hardening and work hardening.

In the strain hardening model, the von Mises equivalent plastic strain

$$\bar{\varepsilon}^p \equiv \int_0^t \sqrt{\frac{2}{3}\dot{\boldsymbol{\varepsilon}}^p : \dot{\boldsymbol{\varepsilon}}^p}dt = \int_0^t \sqrt{\frac{2}{3}}||\dot{\boldsymbol{\varepsilon}}^p||dt. \tag{2.24}$$

and the rate evolution form can be

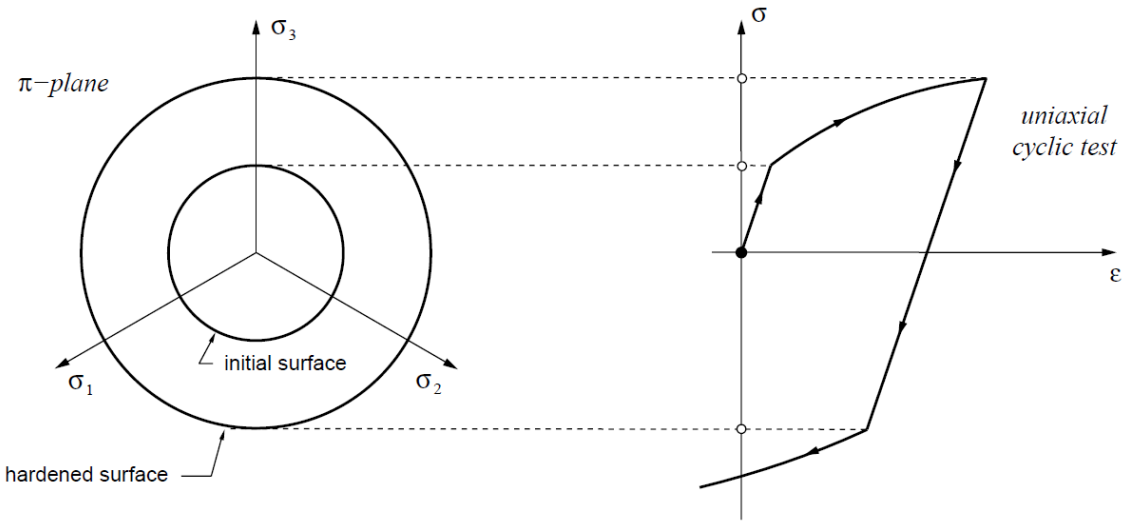

Fig. 2.2 The isotropic hardening behavior.

$$\dot{\bar{\varepsilon}}^p = \sqrt{\frac{2}{3}\dot{\boldsymbol{\varepsilon}}^p : \dot{\boldsymbol{\varepsilon}}^p} = \sqrt{\frac{2}{3}}\|\dot{\boldsymbol{\varepsilon}}^p\| \tag{2.25}$$

2.2.2 Strain-rate-dependent plasticity

The elasto-plastic constitutive theories discussed in previous sections are rate-independent, which means the deformation behavior is independent of the loading rate or time-scale in considered problem. But the rate-dependent deformation behavior of real materials was observed in some situation, like metals, polymers, and composites under some practical circumstances. The schematic diagram of different rate-dependent behavior is shown in **Fig. 2.3**. The typical stress – strain curves at high temperature with different strain-rate were shown in **Fig. 2.3** (a), it is clear that the elastic modulus are rate-independent while the initial yield and hardening curve are strongly depend on strain-rate. In the deformation processing of metal, the working temperature is higher than one-third of the melting point. The deformation behavior is highly affected by process speed, and the rate-dependent plasticity must be considered.

Another well-known time-dependent behaviors of material is creep, which shown in **Fig.**

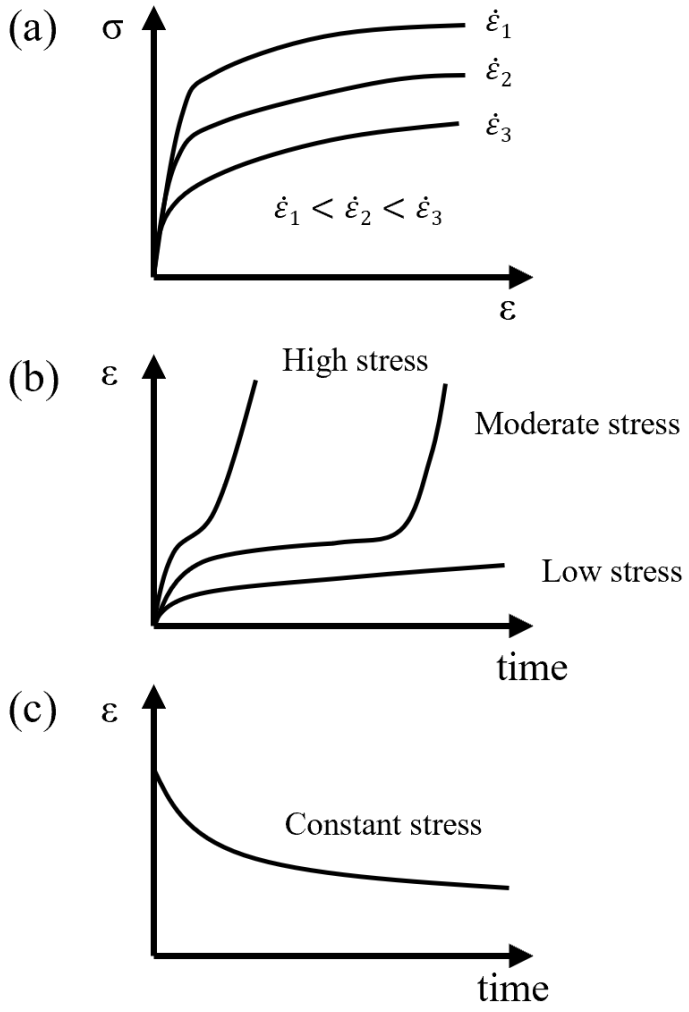

Fig. 2.3 The schematic diagram of strain-rate-dependent plasticity. (a)Strain-rate-dependence. Tensile tests at different strain rates. (b) Creep. Plastic flow at constant stress. (c) Relaxation. Stress decay at constant strain.

2.3 (b). The curves of **Fig. 2.3** (b) show the relationship between strains and time in tensile tests where tensile specimens under different stress levels constantly during long periods of time. At high and moderate stress state, the three states of strain rate changes can be observed. In the first stage, also called primary creep, the strain-rate decrease rapidly and then become steady-state creep, secondary creep, with constant strain rate. In third stage, tertiary creep, the strain rate exponentially increases with time which is normally due to necking , cracks, or voids and leading to fracture. The prediction of creep behavior is crucial in some cases, like the design and analysis of nuclear reactor, jet turbine engineer, and other important components work under harsh environment. The stress relaxation shown in **Fig. 2.3** (c), which is the typical evolution of stress in a relaxation test, is also a important especially in the design of pre-stressed load carrying components.

The strain-rate-dependent plasticity may be important in some situation, and the estimation and prediction is a critical problem in design and process of materials. In order to represent the rate-dependent material response, it is necessary to extend the constitutive model to rate-dependent form.

For example, the rate-independent constitutive model discussed in previous section can be extended to the rate-dependent form with similar format. The usual concept of an elastic domain bounded by a yield surface in the rate-independent theory will remain valid in the visco-plastic case. So the yield function and elastic domain will be

$$\Phi(\boldsymbol{\sigma}, \sigma_y) = q(\boldsymbol{s}(\boldsymbol{\sigma})) - \sigma_y; \quad q = \sqrt{\frac{3}{2}\boldsymbol{s} : \boldsymbol{s}} \tag{2.26}$$

$$\mathcal{E} = \{\boldsymbol{\sigma} | \quad \Phi(\boldsymbol{\sigma}, \sigma_y) < 0\}, \tag{2.27}$$

and the plastic flow rule will be

$$\dot{\varepsilon}^p = \dot{\gamma}\frac{\partial \Phi}{\partial \boldsymbol{\sigma}} = \dot{\gamma}\sqrt{\frac{3}{2}}\frac{\boldsymbol{s}}{||\boldsymbol{s}||} \tag{2.28}$$

$$\dot{\gamma} = \begin{cases} \frac{1}{\mu}\left[\left(\frac{q}{\sigma_y}\right)^{1/\epsilon} - 1\right] & \text{if} \quad \Phi(\boldsymbol{\sigma}, \sigma_y) \geq 0 \\ 0 & \text{if} \quad \Phi(\boldsymbol{\sigma}, \sigma_y) < 0 \end{cases} \tag{2.29}$$

This von Mises-type visco-plastic constitutive model can reproduce the rate-dependent behavior of materials and the examples of stress relaxation and strain-rate dependent stress are shown in **Fig. 2.4**.

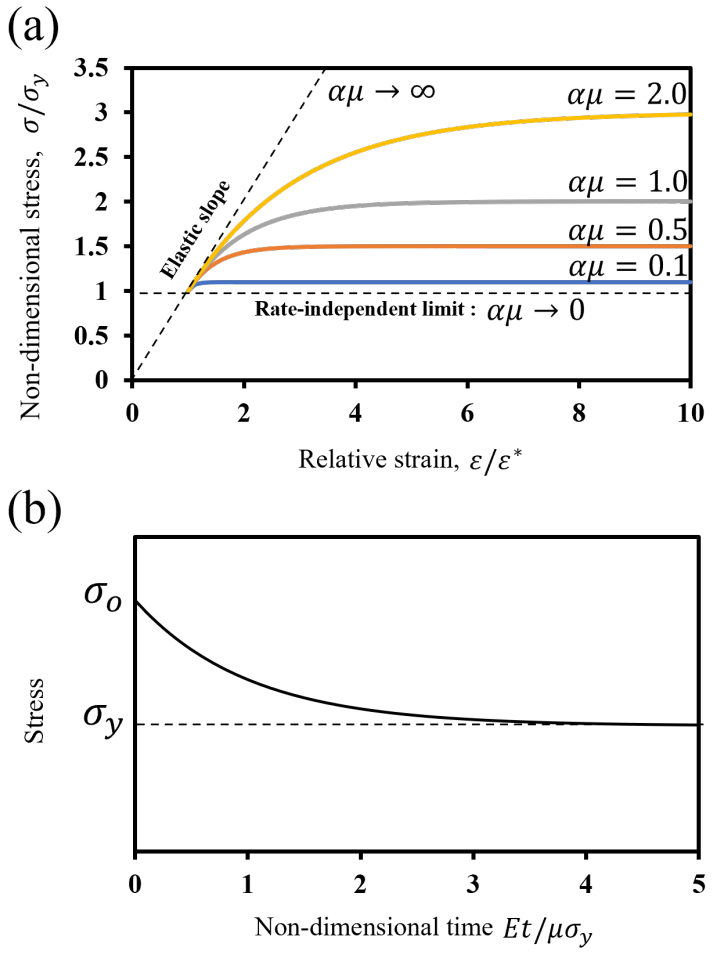

Fig. 2.4 The examples of visco-plasticity model. (a)Strain-rate-dependence. (b) stress Relaxation.

2.2.3 Elasto-plastic constitutive model

An isotropic elasto-plastic constitutive model was employed in this study, which is characterized by the St. Venant elasticity and metal plasticity based on the von Mises yield criterion and power-law hardening. The isotropic elasticity includes the Young's modulus E and Poisson's ratio ν. The equivalent stress–strain relationship can be described as follows:

$$\begin{cases} \sigma^* = E^* \varepsilon^* & \text{if } \sigma^* < \sigma_Y \text{ (elasticity)} \\ \sigma^* = K(\varepsilon^*)^n & \text{if } \sigma^* = \sigma_Y \text{(elasto-plasticity)}, \end{cases} \tag{2.30}$$

where σ^*, ε^*, E^*, σ_Y, K, and n are the von Mises stress norm, equivalent strain, equivalent elastic modulus, yield stress, plastic coefficient, and work-hardening exponent, respectively. The equivalent strain and equivalent elastic modulus are defined as follows:

$$\varepsilon^* = \sqrt{\frac{2}{3}\text{dev}[\boldsymbol{\varepsilon}] : \text{dev}[\boldsymbol{\varepsilon}]} = \frac{\sigma^*}{E^*} + \xi \quad \text{and} \quad E^* = \frac{3E}{2(1+\nu)}, \tag{2.31}$$

where ε is the strain tensor and $\xi = \varepsilon^* - \sigma^*/E^*$ is the equivalent plastic strain. In Equation (2.30), the continuous condition of the stress and strain states at the initial yield stress σ_0 is written as

$$\sigma_0 = K\left(\frac{\sigma_0}{E^*}\right)^n \quad K = \sigma_0\left(\frac{E^*}{\sigma_0}\right). \tag{2.32}$$

From Equations (2.30) and (2.32), the yield strength σ_Y is calculated as a solution to the following equation:

$$\sigma_Y = \sigma_0^{1-n}\left(\sigma_Y + E^*\xi\right)^n, \tag{2.33}$$

To consider the linear hardening behavior of the materials, the constitutive model can be further modified by introducing the linear hardening coefficient H as follows:

$$\sigma_Y = \sigma_0^{1-n}\left(\sigma_Y + E^*\xi\right)^n + H_p\xi, \tag{2.34}$$

Thus, the constitutive model has five independent material parameters: E, ν, σ_0, n, and H. In this study, ν is assumed to be 0.3 because the Poisson's ratio of alloys has an approximate

value of 0.3 at room temperature [47].

2.2.4 Elasto-visco-plastic constitutive model

The isotropic elasto-plastic constitutive model purposed in previous section is rate independent, but rate-dependent plasticity may become dominant in some situation. So it is necessary to extend the constitutive model to rate-dependent form.The elasticity was set as strain-independent, whereas the plastic constitutive equation was defined in a strain-rate-dependent format. Similar to the previous model, the equivalent stress – strain relationship is expressed as follows:

$$\begin{cases} \sigma^* = E^* \varepsilon^* & \text{if } \sigma^* < \sigma_Y \text{ (elasticity)} \\ \sigma^* = K(\varepsilon^*)^n \Gamma(\dot{\xi}) & \text{if } \sigma^* = \sigma_Y \text{(elasto-visco-plasticity),} \end{cases} \tag{2.35}$$

where Γ and $\dot{\xi}$ are the strain-rate function and equivalent plastic strain rate, respectively. The equivalent strain and equivalent elastic modulus are defined previously in Equation (2.31). In this study, the strain-rate function was defined as

$$\Gamma(\dot{\xi}) = (1-\alpha) + \alpha \left(\frac{\dot{\xi}}{\dot{\xi}_0} \right)^m \quad \alpha \in [0,1], \tag{2.36}$$

where α,$\dot{\xi}_0$ and m are the viscoplastic ratio, reference strain rate, and strain-rate exponent, respectively. Then, Equation (2.35) can be written as

$$\sigma^* = \left(\frac{\sigma^*}{E^*} + \xi \right)^n \left\{ (1-\alpha)K + \alpha K \left(\frac{\dot{\xi}}{\dot{\xi}_0} \right)^m \right\} = \left(\frac{\sigma^*}{E^*} + \xi \right)^n \{K_p + K_{vp} \dot{\xi}^m\}, \tag{2.37}$$

where $K_p = (1-\alpha)K$ and $K_{vp} = \alpha K \dot{\xi}_0^{-m}$. Thus, this constitutive model contains four strain-rate-independent and two strain-rate-dependent material constants at a high temperature: E, ν, K_p, n, K_{vp}, and m. The strain-rate-independent initial yield strength is formulated as $\sigma_Y = \left\{ (E^*)^{-n} K_p \right\}^{\frac{1}{1-n}}$. At a high temperature, α can be assumed to be equal to one, i.e., $K_p \equiv 0$. In the special case, a pure-elastic state does not exist.

2.3 Determination of material constants

2.3.1 Determining suitable parameters for inverse estimation

Indentation experiments

Indentations were performed on one grain of the Al–0.1 at%Mg alloy to investigate the experimental variation of the parameters. The sample was annealed at 400 °C in air for 1 h. It was subjected to mechanical polishing, followed by electropolishing to remove the strain induced by mechanical polishing. The average grain size was determined as 99.9 μm based on the EBSD measurement. Indentations at a maximum load of 10 mN were performed at 50 μm intervals as shown in **Fig. 2.5**, using a Hysitron TI 950 TriboIndenter (Bruker) and a diamond Berkovich indenter with an apex angle of 115°. The AFM measurements were performed with the same Berkovich indenter and apparatus to measure the 3D shapes of the indentation marks. The scanning force and rate were 2 μN and 20 μm/s, respectively. The background of the indentation mark shapes was eliminated by subtracting a plain calculated from all sides. Surface roughness of the sample was also measured using AFM. Its root mean square value was 18.60 nm corresponding to approximately 2% of the maximum indentation depth. The results of 17 indentations performed on one grain oriented along the ¡110¿ direction, the area enclosed by the dashed lines in **Fig. 2.5**, were used in the analysis involving experimental variations to eliminate the orientation [48),49)] and boundary effects [50),2)]. The same indenter and experimental conditions were used in all measurements to eliminate other effects such as tip irregularities and loading rates. The effects of these factors on pile-up behavior have been discussed in previous studies [51)].

Indentation simulation using finite element method

The indentation test was simulated using the commercial finite element method software, ABAQUS ver. 6.14 for sensitivity analysis of the parameters influencing the elastoplastic properties. Most previous studies used a conical indenter model instead of a Berkovich indenter, assuming that both provide the same results [52)], which is not actually true [53),54)].

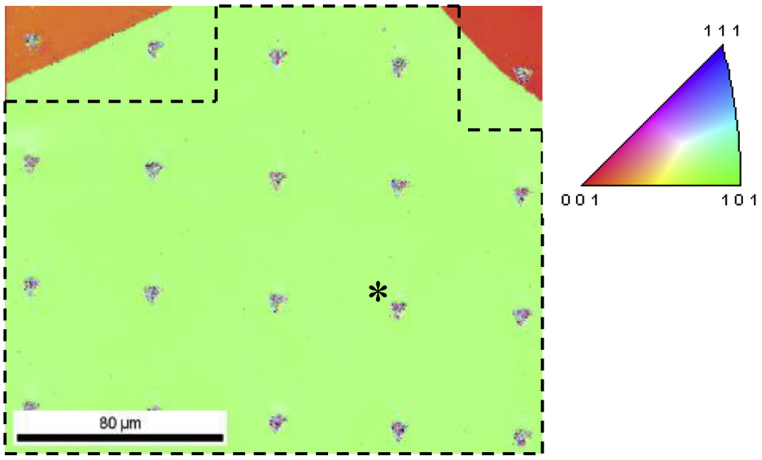

Fig. 2.5 Electron backscatter diffraction map after indentation; 17 indentations on one grain in the area enclosed by dashed lines were used for analyzing experimental variations. [1)]

Moreover, the shape of the indentation mark was considered important in this study, which is different with different shapes of indenters. Therefore, we used the Berkovich indenter model. The analytical model consists of a y-symmetrical sample part and Berkovich indenter part, as shown in **Fig. 2.6**. The size of the sample part is 48.6×24.3×24.3 μm. It has 15,358 nodes and 14,138 elements of an eight-node hexahedron element with reduced integration and hourglass control (C3D8R). The mesh size was decreased in the region underneath the indenter, where the smallest size was 0.3 μm. The symmetrical boundary condition was applied to the xz plane of the sample part, and its bottom was fixed. The Berkovich indenter with an apex angle of 115° and a height of 1.5 μm was generated as a rigid body assuming that the stiffness of the indenter is much higher than that of the sample and that its deformation is negligible. The indentation was simulated by displacing the indenter by 1 μm (= h_{max}) in the z-direction in the loading step, followed by the unloading step in which its position was restored. Frictionless contact was assumed between the indenter and sample, where the effect of friction on the indentation results is insignificant in the case of this apex angle [55),33),56)]. As constitutive equations, Hooke's law and Mises-type rate-independent plasticity were used for elastic and plastic deformation, respectively. The Young's modulus

E, was set at 70 GPa, which is the Young's modulus of aluminum [57]. The initial yield stress σ_Y, and strain hardening exponent n, were parametrically varied in the ranges of 100–1000 MPa and 0–0.5, respectively. The Poisson's ratio ν, was fixed as 0.3 in this study. $\nu \approx 0.3$ in most metals, for example, 0.31 for aluminum alloys and 0.33 for steel [47], and previous studies [27),58)] reported that ν is a minor factor. The analyses were also performed at E = 50 or 200 GPa because many common metals have E values in this range, for example, titanium (E ≈106 GPa), copper (E ≈130 GPa), and steel (E ≈200 GPa).

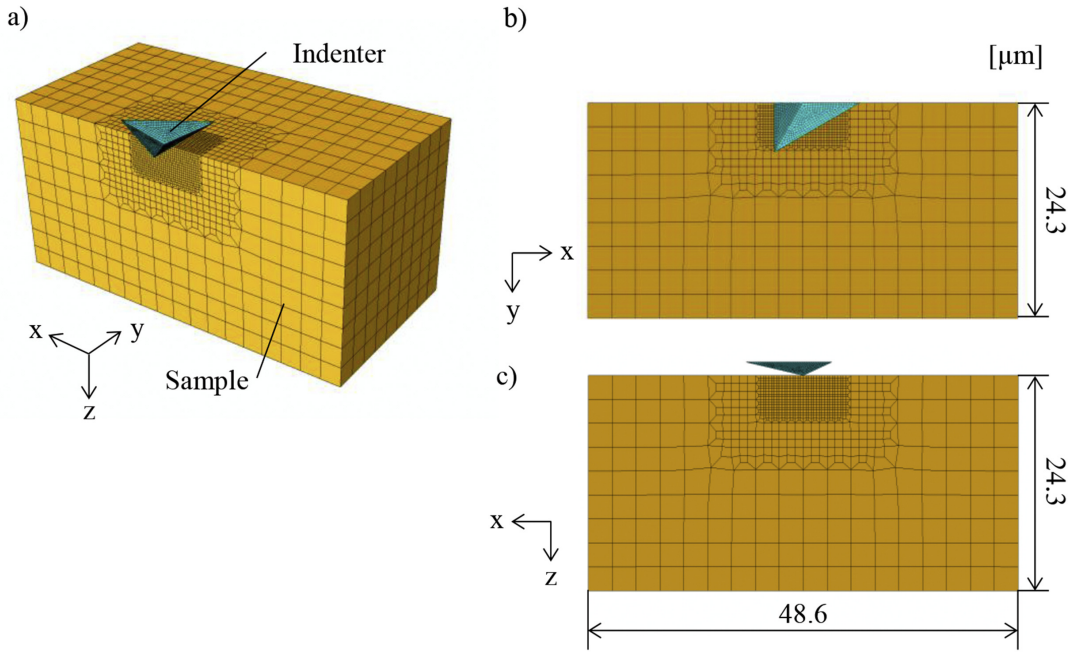

Fig. 2.6 Analytical model of Berkovich indenter: a) perspective view, b) top view, and c) side view. [1)]

Experimental variations

Fig. 2.7 shows the load-displacement curve and indentation mark shape at the position marked with "*" in **Fig. 2.5**. The maximum depth hmax was 0.980 μm. Four parameters were extracted from the load-displacement curve: the coefficient of a parabolic curve during loading, C, ratio of the plastic to the total work, W_p/W_t, indentation hardness H_it and contact stiffness S. W_t and W_p were calculated by integrating the loading curve and subtracting

the integral value of the unloading curve, We, from W_t ($W_p = W_t - W_e$), as shown in **Fig. 2.7** (a). From the indentation mark shapes, two parameters were extracted: the maximum height of the pile-up Z_max and horizontal distance between the positions at the maximum and minimum heights ΔXY. These parameters of the indentation mark were normalized using the maximum indentation depth h_{max}. In **Fig. 2.7**, C =10.4 GPa, W_p/W_t =0.0505, H_{it} =0.414, S =436 mN/μm, Z_{max}/h_{max} =0.116, and $\Delta XY/h_{max}$ =3.44. **Table 2.1** lists the average values, standard deviations, and coefficients of variation (CVs) of the parameters χ, calculated from the 17 indentation results. The CV was calculated by dividing the average value by the standard deviation. A larger CV represents a wider variation in the experiments, indicating low reliability. For the four parameters obtained from the load-displacement curve and $\Delta XY/h_{max}$, the CV was approximately 0.04, while it was larger for Z_{max}/h_{max}.

Table 2.1 Variation of parameters extracted from load-displacement curves and indentation marks in experiment.[1)]

Parameters, χ	Average value	Standard deviation	Coefficient of Variation, CV [-]
C	10.0 GPa	0.4 GPa	0.04
W_p/W_t	5.1×10^{-2}	0.23×10^{-2}	0.045
H_{it}	0.401 GPa	0.018 GPa	0.045
S	$4.22 \times 10^5 \mu N/\mu m$	$0.18 \times 10^5 \mu N/\mu m$	0.043
Z_{max}/h_{max}	0.129	0.012	0.092
$\Delta XY/h_{max}$	3.33	0.13	0.039

Sensitivity analysis

From the indentation simulation, we obtained the load-displacement curves and indentation mark shapes, and then, extracted the parameters as discussed in Section 2.3.1 . **Fig. 2.8** shows the variations of the indentation parameters with the initial yield stress σ_Y and the strain hardening exponent n at E = 70 GPa. Similar distributions were obtained regardless of E except for $\Delta XY/h_{max}$. C gradually increased with σ_Y and n. The distribution indicates

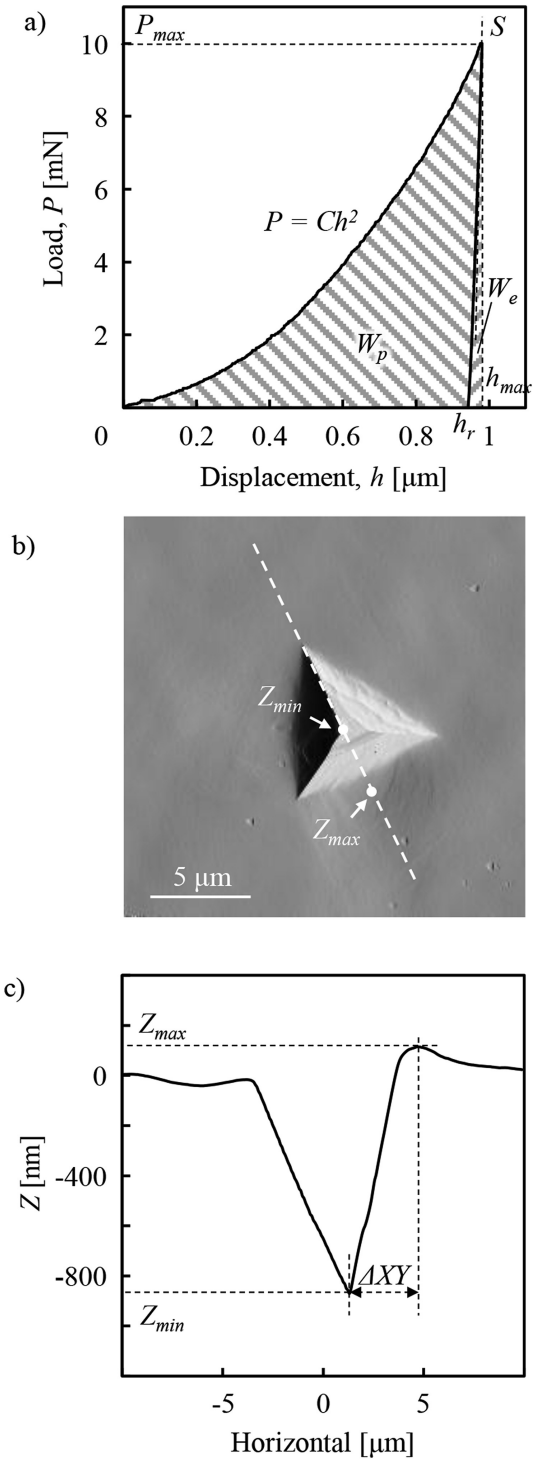

Fig. 2.7 Indentation result at position marked with "*" in **Fig. 2.5**: (a) load-displacement curve, (b) indentation mark, and (c) cross section of indentation mark. [1)]

that the combinations of σ_Y and n giving the same C exist indefinitely and a unique solution for σ_Y and n cannot be determined from one value of C. W_p/W_t and H_{it} have similar distributions to C. Therefore, unique plastic properties cannot be obtained even if two parameters among C, W_p/W_t, and H_{it} are used in the inverse estimation process. The contact stiffness S showed the different distribution from C, W_p/W_t and H_{it}. It increased as σ_Y and n decreased, depending more strongly on n. Since the different distribution of the parameter provides the candidate sets of σ_Y and n, therefore, it is possible to determine a unique solution of plastic properties with the indentation work and S, as Ogasawara et al. [59] proposed. S increases with the contact size between the tip and sample according to $S = (2/\sqrt{\pi})\sqrt{A}E_r$ [10]. Therefore, the increase in S indicates the occurrence of pile-up behavior. The distributions of the parameters extracted from the indentation mark shapes were different from those of the parameters obtained from the P–h curve. Z_{max}/h_{max} strongly depended on n. It increased with the decrease in n, and its rate of change was large at small n. This tendency agrees with the results by Bolshakov and Pharr [27]. $\Delta XY/h_{max}$ showed different distributions at different E values, and its variation was not monotonic. The contour images of the equivalent plastic strain are shown in **Fig. 2.9**. The distribution shape of the plastic strain does not significantly change with the initial yield stress, while its amount increases with the decrease in σ_Y. On the other hand, the strain hardening exponent affects the distribution shape. The plastic strain spread hemispherically at high n, while the distribution was shallow at low n because the plastic strain was concentrated just beneath the indenter owing to the absence of strain hardening. Therefore, the sample region extruded by the indenter appears as a pile up. This is why Z_{max}/h_{max} shows a stronger dependency on n compared to σ_Y. To qualitatively evaluate the sensitivity of parameters χ obtained from the indentation results presented in **Table 2.1**, its gradient $|\Delta\chi'|$ and angle θ in the distributions were defined. First, χ, σ_Y, and n were normalized using their average or maximum values as follows:

$$\chi' = \frac{\chi}{\chi_{ave}}, \sigma'_Y = \frac{\sigma_Y}{\sigma_{Ymax}}, \text{and} \quad n' = \frac{n}{n_{max}}, \tag{2.38}$$

where the prime represents the normalized value, and the subscripts max and min repre-

sent the maximum and minimum values in the range of the parametric study, for example, σ_{Ymin} and σ_{Ymax} =100 and 1000 MPa, respectively. The gradient and its angle were calculated using Eqs. 2.39, 2.40, 2.41, and 2.42.

$$\frac{\Delta\chi'}{\Delta\sigma'_Y} = \frac{\chi'|_{\sigma_{Ymax},n_{min}} - \chi'|_{\sigma_{Ymin},n_{min}}}{\sigma'_{Ymax} - \sigma'_{Ymin}}, \tag{2.39}$$

$$\frac{\Delta\chi'}{\Delta n'} = \frac{\chi'|_{\sigma_{Ymin},n_{max}} - \chi'|_{\sigma_{Ymin},n_{min}}}{n'_{max} - n'_{min}}, \tag{2.40}$$

$$|\Delta\chi'| = \sqrt{\left(\frac{\Delta\chi'}{\Delta\sigma'_Y}\right)^2 + \left(\frac{\Delta\chi'}{\Delta n'}\right)^2}, \tag{2.41}$$

and

$$\theta = \tan^{-1}\left(\frac{\Delta\chi'}{\Delta n'} \Big/ \frac{\Delta\chi'}{\Delta\sigma'_Y}\right) \tag{2.42}$$

For example, in the case of C at E = 70 GPa,

$$\frac{\Delta C'}{\Delta\sigma'_Y} = \frac{57.30 - 8.77}{52.22} \Big/ \frac{1000 - 100}{1000} = 1.03$$

$$\frac{\Delta C'}{\Delta n'} = \frac{38.30 - 8.77}{52.22} \Big/ \frac{0.5 - 0}{0.5} = 0.566$$

$$|\Delta\chi'| = \sqrt{1.03^2 + 0.565^2} = 1.18$$

$$\theta[^\circ] = \tan^{-1}\frac{0.566}{1.03} = 28.7$$

$|\Delta\chi'|$ and θ are listed in **Table 2.2**. C, W_p/W_t, and H_{it} have values similar to $|\Delta\chi'|$ and θ. It was found that the parameters of the indentation mark shape have a larger $|\Delta\chi'|$ than that of the P–h curve, indicating they are more sensitive to plastic properties. θ values of S, Z_{max}/h_{max}, and $\Delta XY/h_{max}$ are more than 15° higher than those of the other parameters, which means these parameters have dependencies on plastic properties different from the other parameters. The

tendencies of $|\Delta\chi'|$ and θ agree with the distribution in **Fig. 2.8**; therefore, the distributions are successfully expressed using $|\Delta\chi'|$ and θ. The same tendencies were also obtained at E =50 and 200 GPa.

Table 2.2 Sensitivity of parameters.[1)]

Parameters, χ	$\|\Delta\chi'\|$ [-]	θ[°]	$\|\Delta\chi'\|$/CV [-]
C	1.18	28.7	27.7
W_p/W_t	1.20	31.6	26.3
H_{it}	1.16	27.8	26.2
S	0.467	56.3	11.0
Z_{max}/h_{max}	3.94	62.7	42.9
$\Delta XY/h_{max}$	0.557	66.0	14.3

Determination of parameters for inverse estimation

To determine the parameters for use in the inverse estimation of plastic properties, an index $|\Delta\chi'|$/CV was introduced. A parameter with large $|\Delta\chi'|$/CV has higher sensitivity compared to its experimental variation, and the estimated elastoplastic property has high precision. In contrast, when $|\Delta\chi'|$/CV is small, the estimated plastic properties may be wrong owing to experimental errors. The calculated $|\Delta\chi'|$/CV is also listed in **Table 2.2**. C, W_p/W_t, and Hit have similar values of $|\Delta\chi'|$/CV and θ. C and W_p/W_t (or other ratios of the indentation work) were used for inverse estimation in most previous studies employing the representative strain technique. According to the present analysis, the same estimation result is obtained no matter which parameter, C or W_p/W_t, is used in inverse estimation. Here, the $|\Delta\chi'|$/CV value of C is used as a criterion to judge whether a parameter is suitable for use in inverse estimation. $|\Delta\chi'|$/CV values of S was less than half that of C. The sensitivity of S is small though its experimental variation is comparable to that of C and W_p/W_t, which implies that an estimation result calculated from S has small accuracy. In the case of $\Delta XY/h_{max}$, $|\Delta\chi'|$/CV was comparable to that of S at E =50 and 70 GPa, while it was larger than that of C at

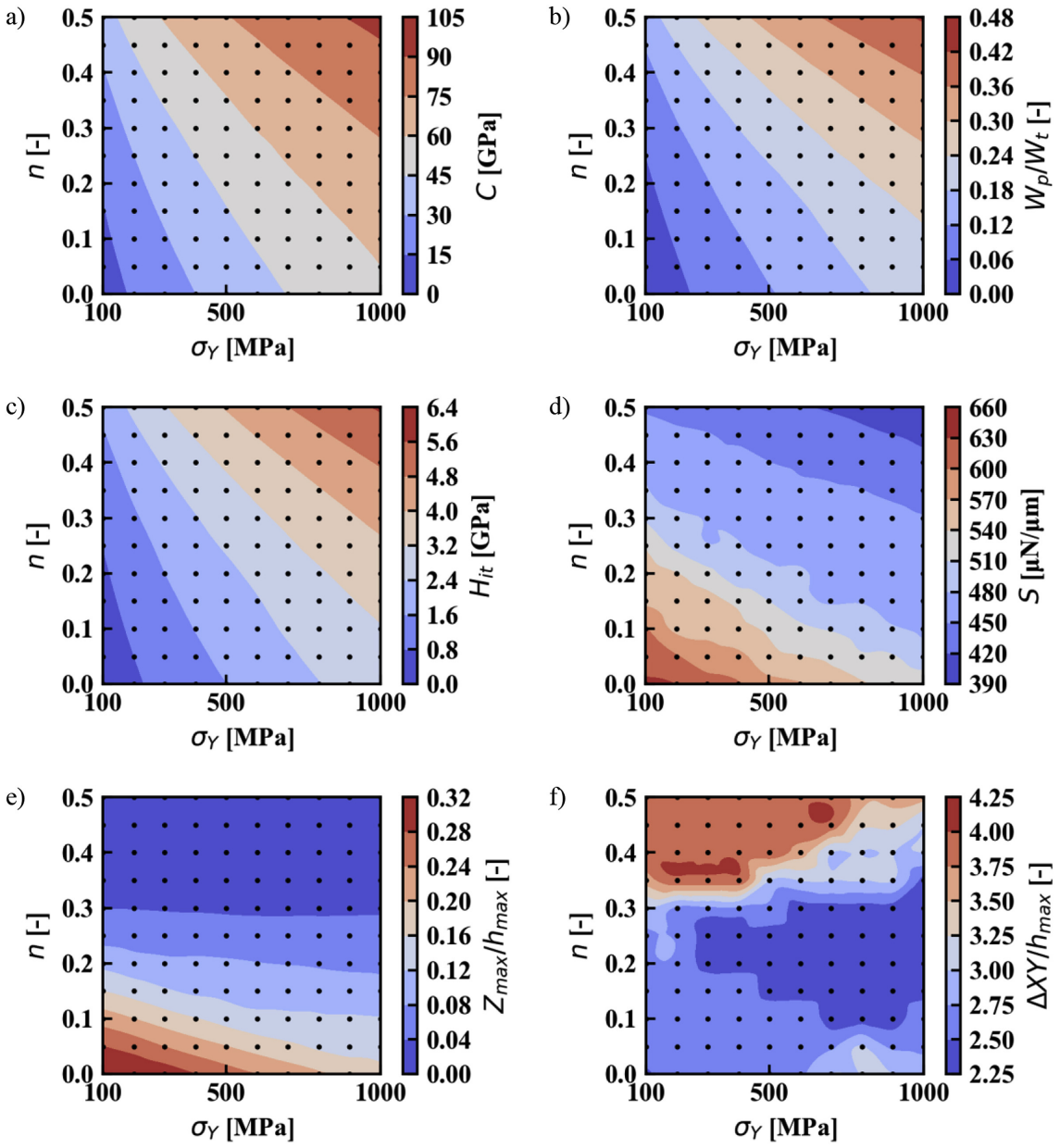

Fig. 2.8 Dependence of indentation parameters on initial yield stress σ_Y and strain hardening exponent n at $E = 70$ GPa: (a) C, (b) W_p/W_t, (c) H_{it}, (d) S, (e) Z_{max}/h_{max}, and (f) $\Delta XY/h_{max}$; color maps were constructed from the values at every plot where the indentation simulation was performed. [1)]

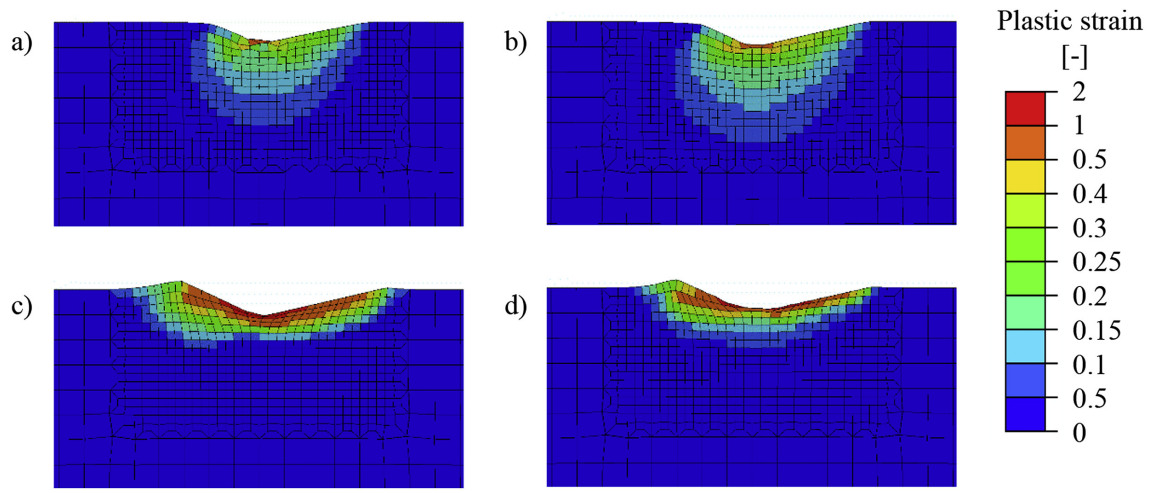

Fig. 2.9 Contour images of equivalent plastic strain beneath indenter at E = 200 GPa: (a) σ_Y = 100 MPa, n = 0.5, (b) σ_Y = 1000 MPa, n = 0.5, (c) σ_Y = 100 MPa, n = 0.0, and (d) σ_Y = 1000 MPa, n = 0.0. [1)]

E =200 GPa, resulting in an imprecise result at the low Young's modulus. Z_{max}/h_{max} has a larger $|\Delta\chi'|$/CV than C despite its large CV because its sensitivity is high. Therefore, it is evident that plastic properties are estimated with less error using Z_{max}/h_{max}. In addition, its θ and distribution are different from those of C. Hence, Z_{max}/h_{max} was the parameter used for inverse estimation in addition to C. It is expected that the estimation precision is higher at smaller n because its rate of change was large. This concept was applied to most of the metals as the same tendency was obtained at E =50 and 200 GPa.

2.3.2 Neighboring indentation test

The neighboring indentation method was proposed to estimate the plastic material properties based on the interaction effect between two indentations at neighboring positions.

Concept

In instrumented indentation tests or hardness tests for alloys, the influence region of the residual stress and plastic deformation can be regarded as approximately two times larger

than the size of the indentation impression. Typically, the spacing between the existing and subsequent indentations is set to be large enough to avoid any interaction between them. Following various standards of instrumented indentation testing [19),20),21)], in a simple case of two indentations of the same depth, the second indentation is generally performed at a position that is located at a distance that is five times of the size of the indentation impression away from the first indentation to avoid overlapping plastic strain zones. Phani and Oliver [60)] argued that the appropriate indentation spacing is over 10 times the indentation depth to avoid the interaction between indentations for a measurement of elastic modulus and hardness based on experiments and finite element simulations.

The effect of plastic deformation history is expected to result in work-hardening which is a fundamental mechanical behavior in metal plasticity. Therefore, the proposed approach makes active use of the interaction between the first and second indentations. In the approach, the second indentation is performed at a position neighboring the first one.In instrumented indentation for alloys, the load– depth curve shown in **Fig. 2.10** is generally assumed to be a quadratic function:

$$P = Ch^2, \tag{2.43}$$

where C is the loading curvature. As mentioned in the introduction, additional data on the loading curvature are required to determine a unique set of material constants of the plastic constitutive model, even for the simplest plastic constitutive model [29),30),31)]. In this study, the loading curvature of the first indentation C_1 and the difference of the curvatures $C_2 - C_1$ are chosen as two response variables characterized by the plastic properties. In this approach, the material constants corresponding to the experimental results of indentation curvatures are determined from the response surfaces, which are prepared using high- throughput simulations based on the finite element method as a material database in advance.

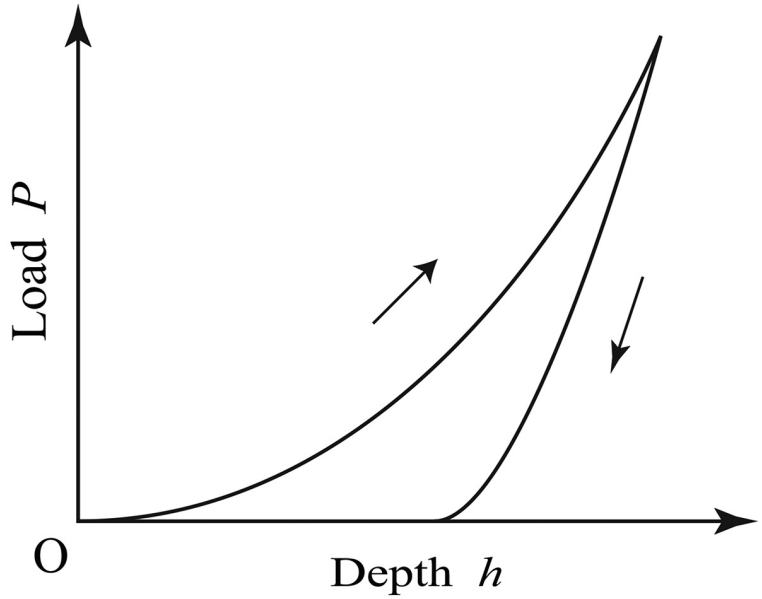

Fig. 2.10 Load–depth curves of the instrumented indentation.

Finite element model

A three-dimensional finite element model was constructed for simulations of neighboring indentation tests, as shown in **Fig. 2.11**, in which a mirror symmetrical boundary condition was applied to the $X - Y$ plane along the center of the object, and the vertical displacement along the bottom of the finite element model was constrained. The finite element model included 38,181 nodes and 35,994 eight-node hexahedral elements with reduced integration, where the contact area between the indenter and sample was more finely discretized than the other area. The Berkovich indenter was assumed to be a rigid body,and the friction between the indenter and sample was not considered in this study. Simulations were per-formed using displacement control at the top of the indenter and solved as quasi-static boundary value problems with an implicit scheme.

Sensitivity analysis

Similar to section 2.3.1, the sensitivity analysis was necessary to find the suitable parameters in neighboring indentation to characterize the elasto-plastic properties. A parametric

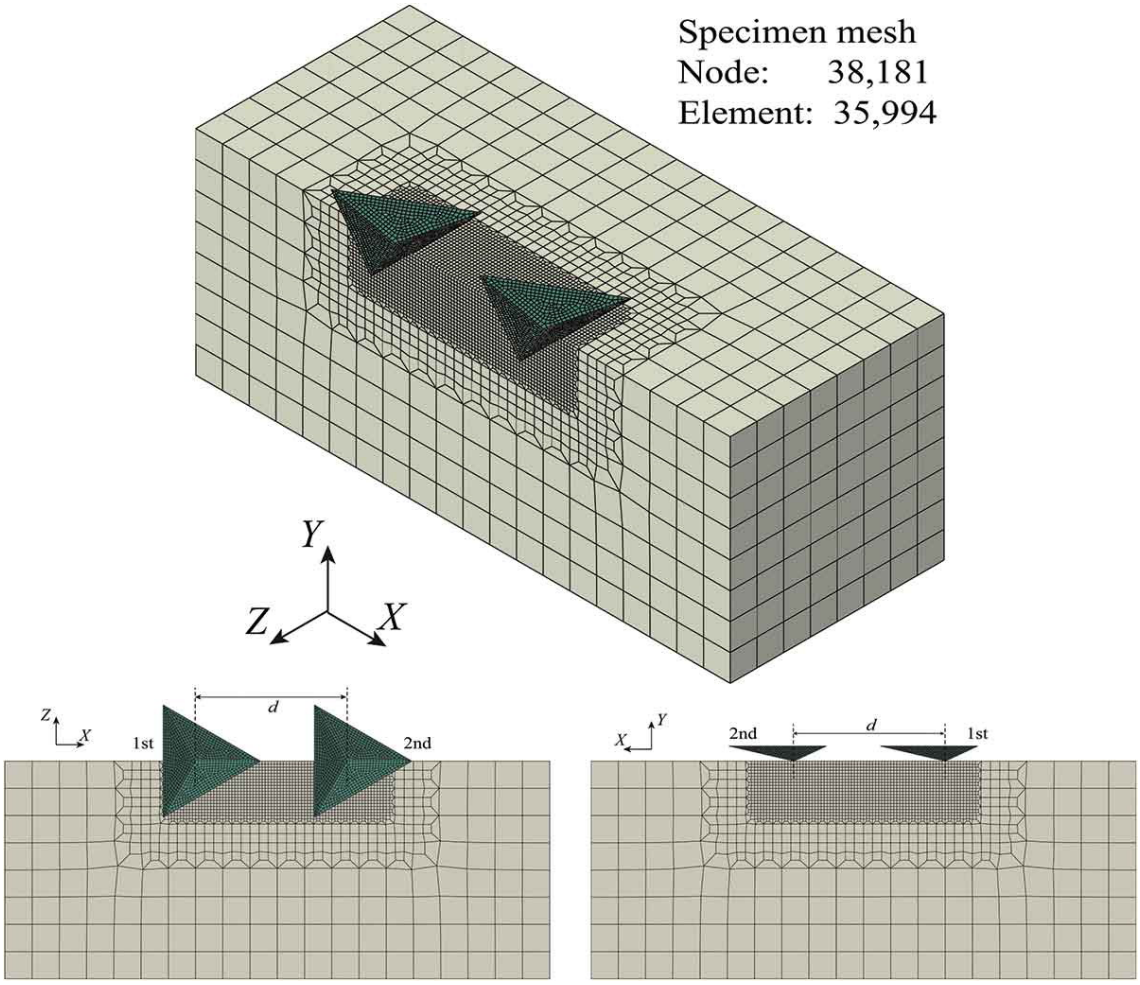

Fig. 2.11 Finite element model of neighboring indentation method.

study of 128 cases was conducted for materials with different combinations of elastoplastic properties at $E = 70$ GPa and 200 GPa, respectively. initial yield strength σ_0 was varied from 100 MPa to 800 MPa, strain hardening exponent n was varied from 0.05 to 0.4, Poisson's ratio was fixed at 0.3. Factors of two $P - h$ curves obtained from neighboring indentation were extracted to discuss its variation at each indentation parameter. **Fig. 2.12** and **Fig. 2.13** shows the variations of the curvature C, hardness H, stiffness S, ratio of the plastic to the total work W_p/W_t, and the curvature difference between two curves be normalized by equivalent Young's modulus $(C_2 - C_1)/E^*$ with variable initial yield stress σ_0 and strain hardening exponent n at $E = 70$ and 200 GPa. Similar distributions can be observed in C, H, and W_p/W_t, while the S and $(C_2 - C_1)/E^*$ show different tendency compare with previous factors. A unique solution of material constants can not be obtained only from those similar factors C, H, and W_p/W_t. For S and $(C_2 - C_1)/E^*$, S is related to the contact radius because of the estimation method discussed in section 1.3.1, $S = (2/B\sqrt{\pi})E_r\sqrt{A_p}$, and it will deviate from the the theoretically value due to pile-up or sink-in phenomenon, which means S is not a suitable parameters for robust estimation method of plastic properties. Therefore, $(C_2 - C_1)/E^*$ was determined as a parameter to characterize the elastoplastic properties of materials. Those factors discussed above shows similar distribution at $E = 70$ and 200 GPa, which means the determined experimental parameters can be used in various alloys.

Numerical examination of indentation conditions

In the proposed approach, the indentation conditions such as the position and depth of the second indentation must be appropriately designed to robustly determine the plastic properties of various alloys. This is because the plastic deformation underneath the indentations depends on both elastic and plastic material properties [60]. In this part, the suitable condition of the neighboring indentation method was numerically examined using finite element simulations.A series of simulations were performed to investigate the suitable position and depth of the second indentation, where the distance between the first and second indentations d and the maximum depth of the second indentation h_2 for the maximum depth of the first inden-

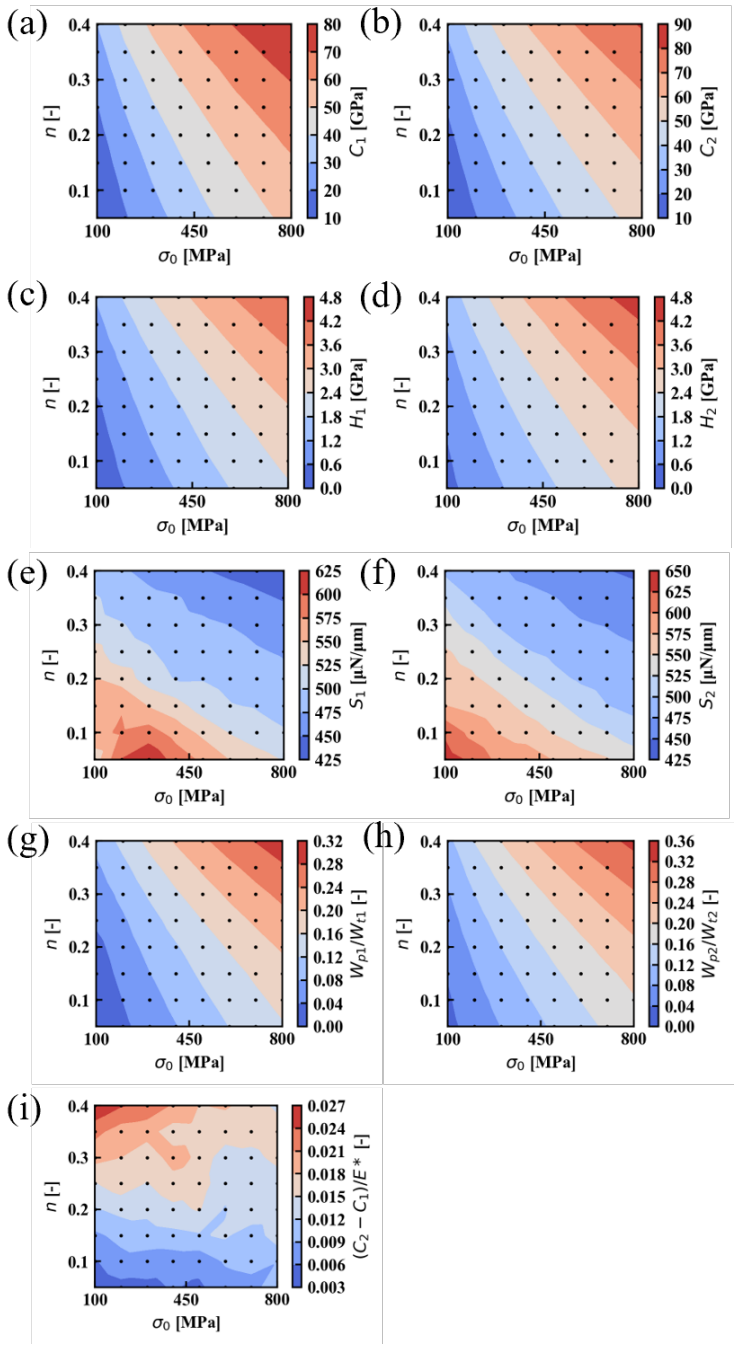

Fig. 2.12 Variation of indentation parameters on initial yield stress σ_0 and strain hardening exponent n at E=70 GPa, $(h_2/h_1, d/l) = (1.0, 1.2)$: (a) C_1, (b) C_2, (c) H_1, (d) H_2, (e) S_1, (f) S_2, (g) W_{p1}/W_{t1}, (h) W_{p2}/W_{t2}, (i) $(C_2 - C1)/E^*$.

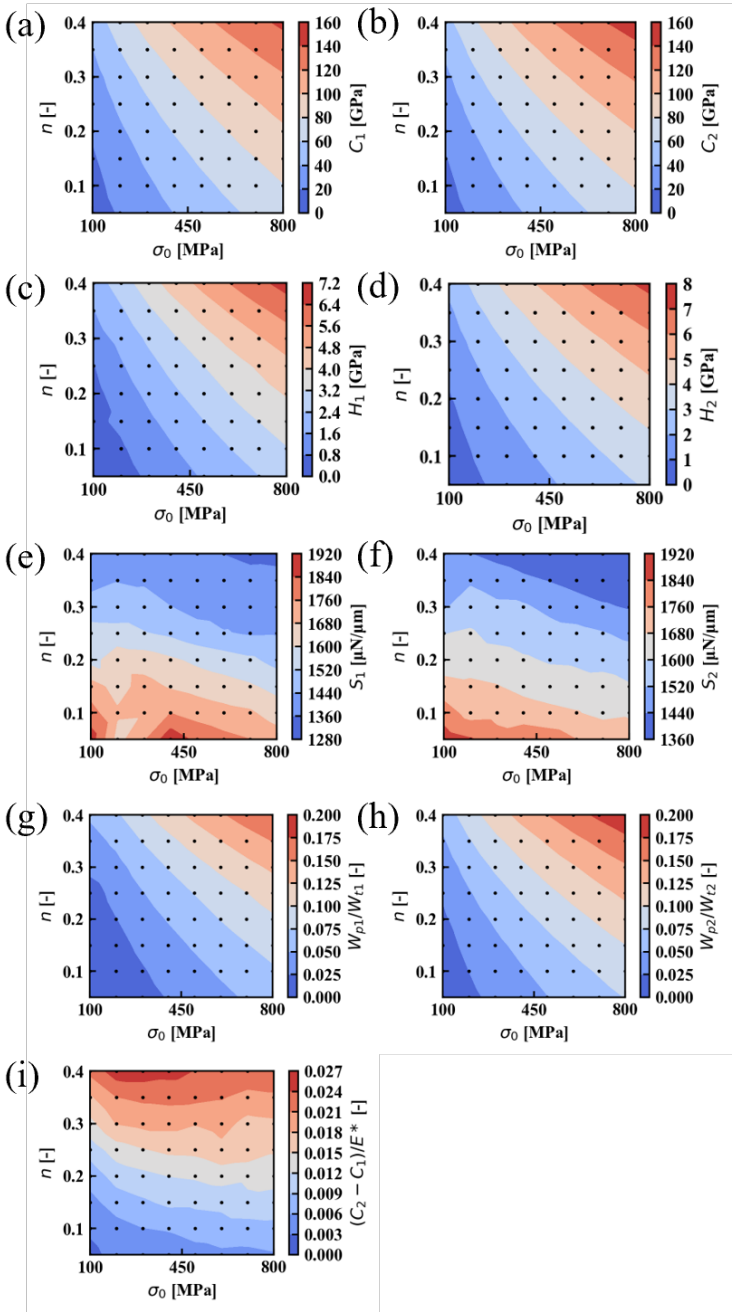

Fig. 2.13 Variation of indentation parameters on initial yield stress σ_0 and strain hardening exponent n at E=200 GPa, $(h_2/h_1, d/l) = (1.0, 1.2)$: (a) C_1, (b) C_2, (c) H_1, (d) H_2, (e) S_1, (f) S_2, (g) W_{p1}/W_{t1}, (h) W_{p2}/W_{t2}, (i) $(C_2 - C1)/E^*$.

tation h_1 were examined. h_1 was set to 1 μm for the simulations. The indentation spacing d must be as small as possible, while the maximum depth of the second indentation h_2 must be as large as possible. Therefore, the following two cases were compared:

$$(d/l, h_2/h_1) = \begin{cases} (1.2, 1.0) & : \text{case(i)} \\ (1.5, 1.2) & : \text{case(ii)} \end{cases} \tag{2.44}$$

where the spacing and depth were normalized to $d = l$ and $h_2 = H_1$ by the horizontal impression size l and the maximum depth of the first indentation h_1 , respectively. Based on the geometry of a triangular pyramidal indenter shown in **Fig. 1.4**, the impression size l was calculated for a depth h_1 as follows:

$$l = (\tan\theta_1 + \tan\theta_2)h_1 = 6.51h_1, \tag{2.45}$$

where $(\theta_1, \theta_2) = (77.0°, 65.3°)$ for the Berkovich indenter. In case (i), a second indentation was per-formed at the same depth as that of the first indentation. In case (ii), the depth of the second indentation was higher than that of the first indentation, but it was located farther away than in case (i). It is noted that the spacings d were defined to be large enough to avoid the effect of the surface deformation around the impression of the first indentation.

The response variables C_1 and $C_2 - C_1$ in the two cases of Equation (2.44) were calculated in the range of $\sigma_0 \in [100\text{MPa}, 700\text{MPa}]$ and $n \in [0.05, 0.35]$ for two Young's modulus $E =$ 70 GPa and 200 GPa, which are the moduli of aluminum alloy and steel, respectively. The distributions of the response variables are shown in **Fig. 2.14** and **Fig. 2.15**, where the variables were normalized by the equivalent Young's modulus E^*. Based on the calculated mesh data (4×4), the response surfaces were drawn with a bilinear interpolation function. The calculated points were indicated by dots in **Fig. 2.14** and **Fig. 2.15**. In these finite element analyses, 16 calculations were performed for each case. The process required 30 hours because the typical CPU time of a single simulation was approximately 2 hours.

The plastic strain distributions after the second indentation and load–displacement curves of the two indentations are shown in **Fig. 2.16** as representative results of finite element simulations for the two sets of material constants at $E = 70$ GPa. The plastic strain was distributed

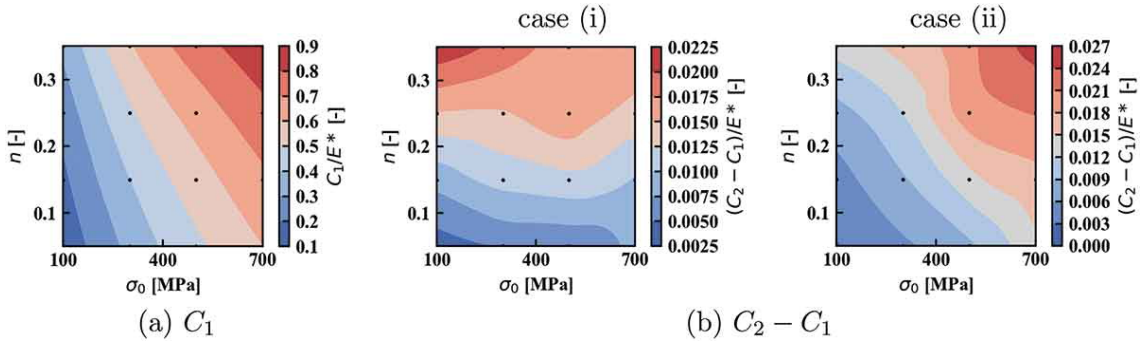

Fig. 2.14 Numerical examination: Response surface of loading curvature in the case of E = 70 GPa.

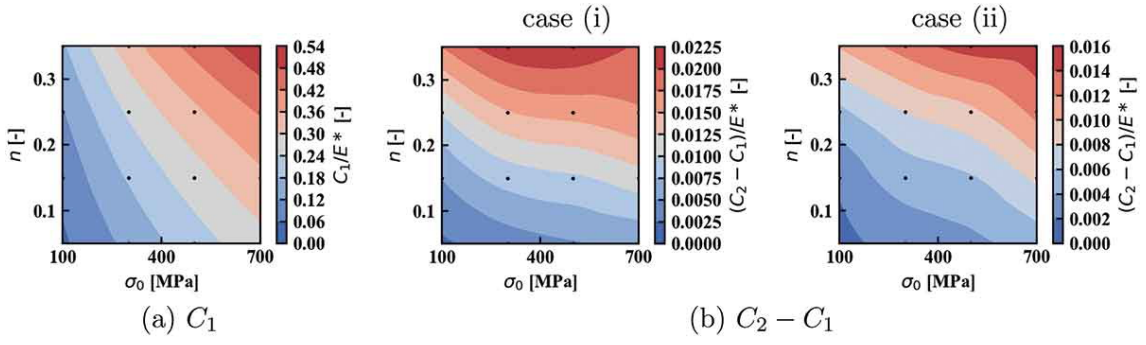

Fig. 2.15 Numerical examination: Response surface of loading curvature in the case of E = 200 GPa.

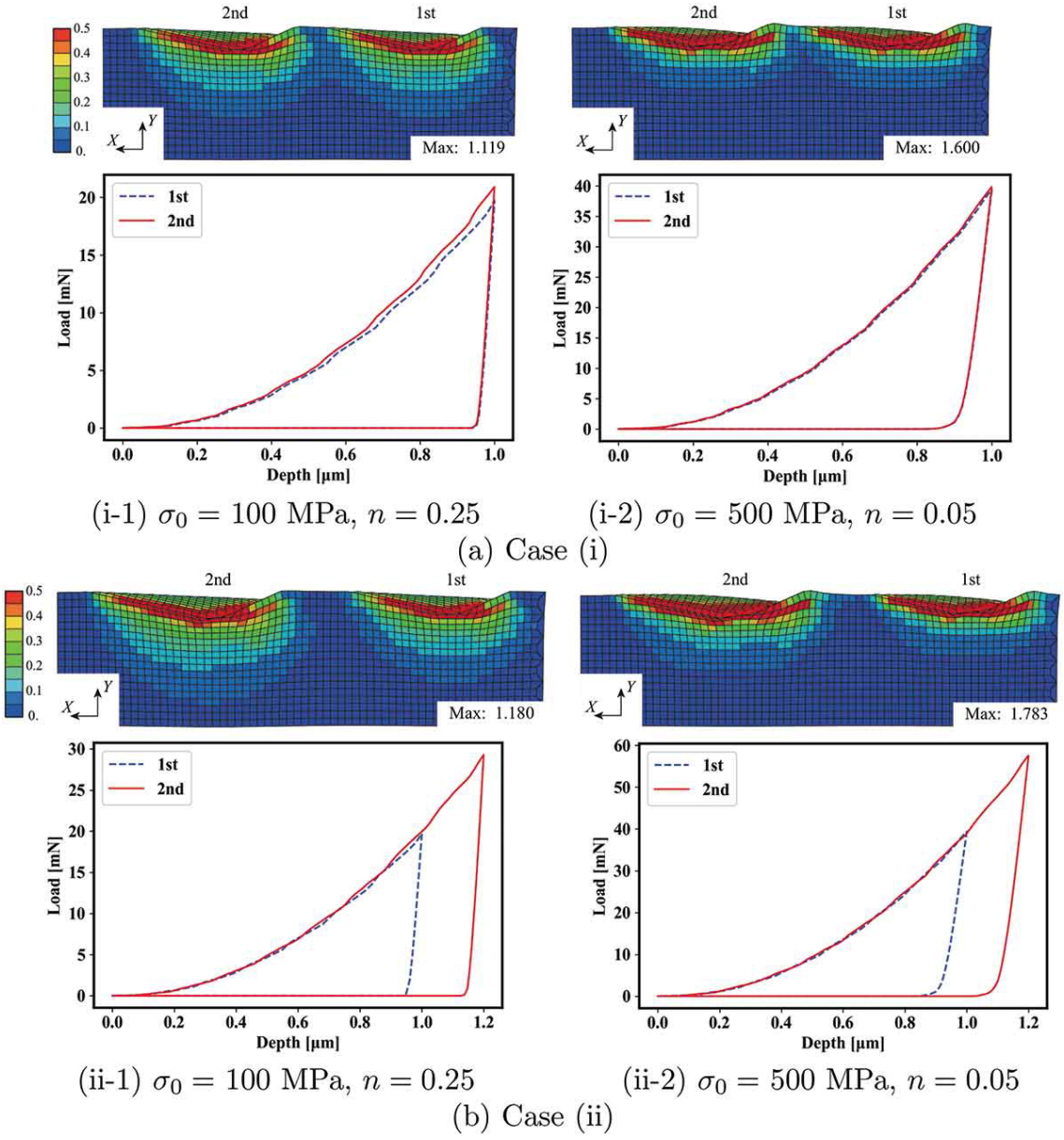

Fig. 2.16 Distribution of equivalent plastic strain under two indentations and its load-depth curves at E = 70 GPa.

without a blank in both simulations of case (i); in contrast, in case (ii), the distribution of plastic strain was discontinuous or the overlapping area of plastic strain was very small. As a result, the response variable $C_2 - C_1$ is relatively small in case (ii). To obtain a unique solution with the neighboring indentation method, the important features of the response surfaces are as follows:

- The response surface is smooth and has a large difference between the maximum and minimum values.
- The two response surfaces have a different tendency.

From the above aspects, the case of $(h_2/h_1, d/l) = (1.0, 1.2)$, in which the depths of the two indentations were the same, is better for indentation conditions. Moreover, this case is preferable for experiments because of the simple operation of the equipment.

2.4 Solution methods

From the instrumented indentation test, the experimental material response can be characterized by the *P*–*h* curves, topography of indentation impression and $C_2 - C_1$. To determined the material constants from these results, various solution methods have been used in this study.

2.4.1 Gradient descent method

To determine the material constants in the constitutive model, optimization algorithm is needed to minimize the difference between the simulation and experimental results. Gradient descent is a iterative optimization algorithm for finding the local minimum of a differentiable function. The first step is to calculate the gradient of the function in initial point, and take step in the opposite direction of the gradient (which is the direction of steepest descent of the function) to the next point. And repeat this method until it reach a local minimum point.

2.4.2 Data-driven method

Another way to determine the material constants from experimental results is to prepare the response surface of material properties in the range we expected in advance. The response surface can be consider as a material database, the experimental results can directly draw the curves on the response surface and the intersection point is the determined constants. The advantage of this method is that it can be prepared in advance and can be used in different materials.

2.5 Summary

The suitable parameters for the inverse estimation from single instrumented indentation test were examined and the curvature of the $P - h$ curve and pile-up topography Z_{max}/h_{max} were chosen. To utilize the interaction between two indentation in neighboring position, neighboring indentation test was purposed and the suitable indentation condition $(h_2/h_1, d/l) = (1.0, 1.2)$ were numerically examined using finite element simulations. To determine the material constants from those experimental results, gradient descent and data-driven method were used. The validation of purposed method will be introduced in the following chapters.

Chapter 3

Validation of estimation methods of plastic properties

3.1 Introduction

In this chapter, the purposed estimation methods of plastic properties using instrumented indentation were validated for application to aluminum alloys and a stainless steel. In section 3.2, the material databases were prepared following the experimental parameters and indentation conditions determined in chapter 2. And the following instrumented indentation tests were performed to determine the material constants in elasto-plastic constitutive model in section 2.2.3. The estimation results based on single indentation with pile-up topography and neighboring indentation test were compared with the experimental tensile test.

3.2 Response surface of indentation parameters

3.2.1 Response surface for neighboring indentation test

Following the numerical examination in section 2.3.2, the response surfaces similar to those in **Fig. 2.14** and **Fig. 2.15** were recalculated based on the neighboring indentation method to develop a material database to determine a set of material constants for the plastic

constitutive model, in which the calculation mesh (8×8) was finer than those of the previous numerical examinations in section 2.3.2. The resulting response surfaces are shown in **Fig. 3.1** and **Fig. 3.2**. The process required approximately 120 hours to produce one set of response surfaces. The database is applicable to the experimental data following the experimental conditions $(h_2/h_1, d/l) = (1.0, 1.2)$. Note that the maximum indentation depth $h_1 = h_2$ should be sufficiently large to eliminate potential errors, including those caused by the geometrical error of the indenter, surface roughness of samples, and nanoscopic strengthening mechanism.

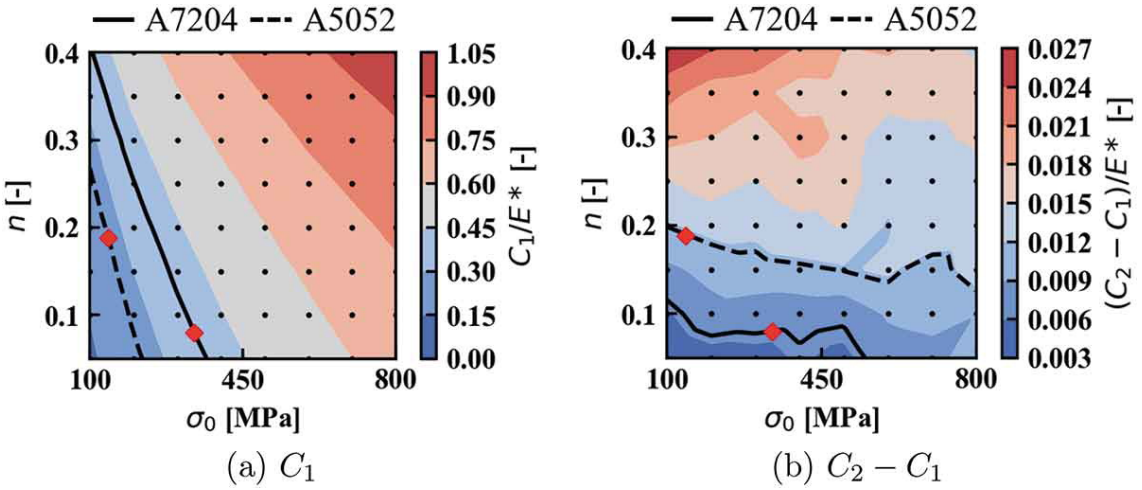

Fig. 3.1 Response surface of loading curvature for $E = 70$ GPa.

The database produced for the neighboring indentation method was validated for application to aluminum alloys and a stainless steel in section (3.3).

3.3 Comparison with tensile test

3.3.1 Estimated from pile-up topography

The elastoplastic properties of the aluminum alloy were estimated from a single indentation result using the parameters obtained from the P–h curve, C, and the indentation mark shape, Z_{max}/h_{max}. An indentation test was performed on the A5052 aluminum alloy polished

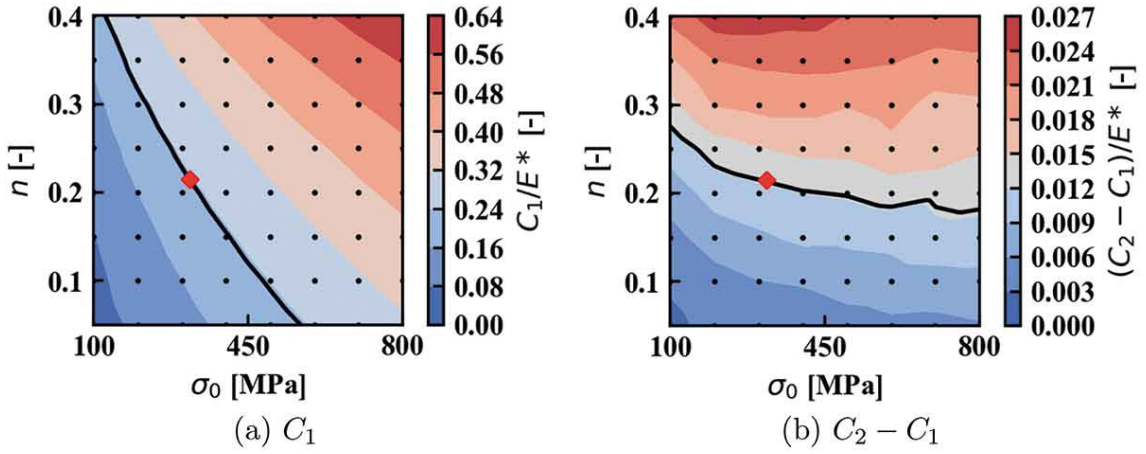

Fig. 3.2 Response surface of loading curvature for E = 200 GPa.

in the same way as that described in Section 2.3.1 using DUH-211 (Shimadzu) with the 115° Berkovich indenter. The maximum load and loading rate were 1000mN and 70.07 mN/s, respectively. The shapes of the indentation marks were measured using a laser microscope (Keyence). From the P–h curve and indentation mark shape, C and Z_{max}/h_{max} were calculated, respectively. A 100° Berkovich indenter was also used on the same sample for dual indenter techniques. The numerical simulation of the indentation test was repeated for inverse estimation. The analytical model used was the same as described in Section 2.3.1. The initial yield stress σ_Y, and strain hardening exponent n, were optimized to reduce the residual error in calculating C and Z_{max}/h_{max}. The Levenberg–Marquardt method [61] was used to solve the optimization problem. A tensile test was performed at a strain rate of $2.4 \times 10^{-4} s^{-1}$ with AG-X (Shimadzu). The stress-strain curves estimated via inverse analysis and of the tensile test are shown in **Fig. 3.3**. The estimated stress-strain curve agrees with the tensile test result, while showing a higher initial yield stress of 214.2 MPa and lower strain hardening exponent of 0.089. **Fig. 3.3** also shows the inverse estimation results using the 115° and 100° indenters, where the dual indenter techniques [62),34)] were used. The strain hardening exponent was estimated as 0 with the latter technique. The single indenter technique using C and Z_{max}/h_{max} provided similar results to the dual indenter technique. It was, therefore, confirmed that the inverse estimation using C and Z_{max}/h_{max} provides plastic properties similar

to those obtained using the dual indentation techniques.

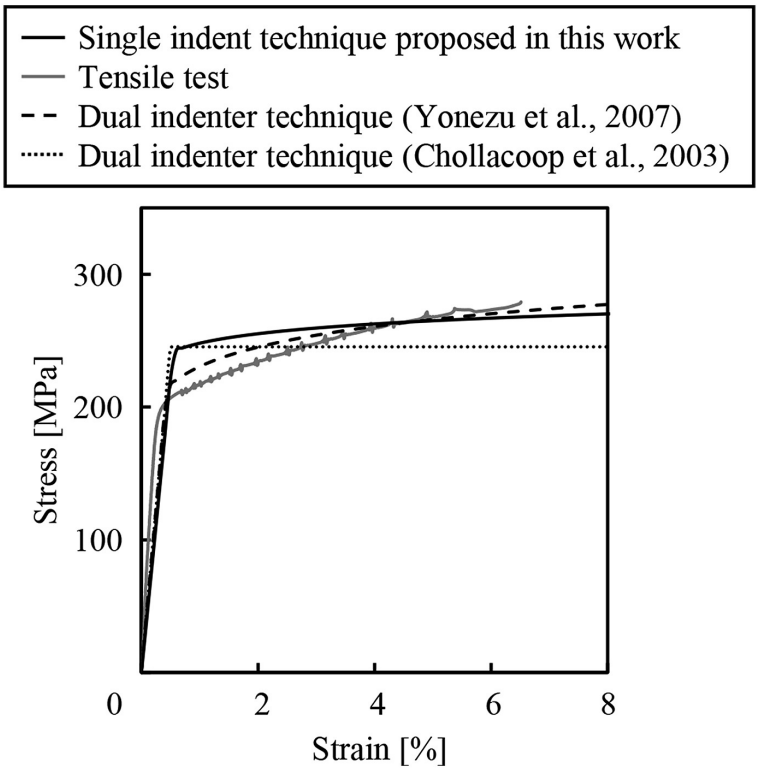

Fig. 3.3 Stress-strain curves of A5052 aluminum alloy obtained from tensile test and inverse estimation techniques. [1)]

3.3.2 Estimated from neighboring indentation test

Experimental parameters

Instrumented indentation tests were performed at room temperature with a TI900 TriboIndenter (Bruker, USA) using a Berkovich indenter for three samples: A5052 and A7204 aluminum alloys and SUS304 stainless steel. The composition of those samples are shown in **Table 3.1–3.3**. Mechanical polishing with diamond and colloidal silica suspensions was conducted on the sample surface, followed by electrical polishing to remove the residual plastic strains. The mechanical polishing condition of both aluminum alloys and stainless steel are shown in **Table 3.4** and **Table 3.5**. Considering the maximum load of the equip-

ment, the maximum indentation depths $h_1 = h_2$ were defined as 8.0, 7.5, and 5.3 μm for A5052, A7204, and SUS304, respectively. Using Equation (2.45), the indentation spacings were set up as 62.5, 58.6, and 41.4 μm for each sample, respectively. The loading and unloading rates of the indentation tests were fixed to 0.1 μm/sec. The neighboring indentation tests were performed five times for each sample and the averaged values were used for the estimation to reduce experimental errors.

Experimental results

The *P–h* curves and indentation impressions of A5052, A7204, and SUS304 are shown in **Fig. 3.4**. The grain size of each sample was over 40 μm, and the neighboring indentation tests were performed for a single or few grains with various crystallographic orientations. We so confirmed that the effect of crystallographic anisotropy of the samples on the *P–h* curves was small in these experiments. The averaged loading curvatures of the five neigh-boring indentation tests and the deviations are shown in **Table 3.6**.

Table 3.1 Alloy composition of the aluminum ally A5052 [wt%].

Zn	Mg	Cr	Cu	Fe	Si	Mn
0.02	2.5	0.18	0.02	0.2	0.09	0.04

Table 3.2 Alloy composition of the aluminum ally A7204 [wt%].

Zn	Mg	Zr	Cu	Fe	Si	Ti
5.60	1.34	0.16	0.15	0.03	0.02	0.02

Table 3.3 Alloy composition of the stainless steel SUS304 [wt%].

C	**Si**	**Mn**	**P**	**S**	**Ni**	**Cr**	**Co**
0.06	0.24	1.12	0.037	0.025	10.08	18.14	0.18

Table 3.4 The mechanical polishing condition of aluminum alloys.

	Polishing cloths	Micron size [μm]	Lubricant	Load/pc [lb]	RPM [Head/Base]	Rotation direction	Time
Gridning	Grit400	22.1	Water	3	60/250	clockwise	0:50
	Grit600	14.5	Water	3	60/250	clockwise	0:30
Polishing	TriDent	9	MetaDi fluid	5	60/150	clockwise	5:00
	VerduTex	3	MetaDi fluid	5	60/150	clockwise	4:00
	MD-Nap	Spray P 1	DP-Lubricant	5	60/150	clockwise	4:00
Final polishing	ChemoMet	MasterMet	Water	5	60/100	counterclockwise	2:00

Table 3.5 The mechanical polishing condition of stainless steel.

	Polishing cloths	Micron size [μm]	Lubricant	Load/pc [lb]	RPM [Head/Base]	Rotation direction	Time
Gridning	Grit320	34.3	Water	4	60/150	clockwise	1:00
	Grit600	14.5	Water	4	60/150	clockwise	1:00
Polishing	TriDent	9	MetaDi fluid	5	60/150	clockwise	10:00
	VerduTex	3	MetaDi fluid	5	60/150	clockwise	8:00
	VerduTex	1	MetaDi fluid	5	60/150	clockwise	8:00
Final polishing	ChemoMet	MasterMet	Water	5	60/150	counterclockwise	3:00

Table 3.6 Averaged loading curvatures and the deviations obtained from five neighboring indentation tests.

Material	C_1 [GPa]	C_2 [GPa]	$C_2 - C_1$
A5052 aluminum	20.49±0.6	21.42±0.46	0.935±0.466
A7204 aluminum	30.71±0.71	31.24±0.89	0.529±0.239
SUS304 stainless steel	54.03±2.52	56.85±2.93	2.825±1.822

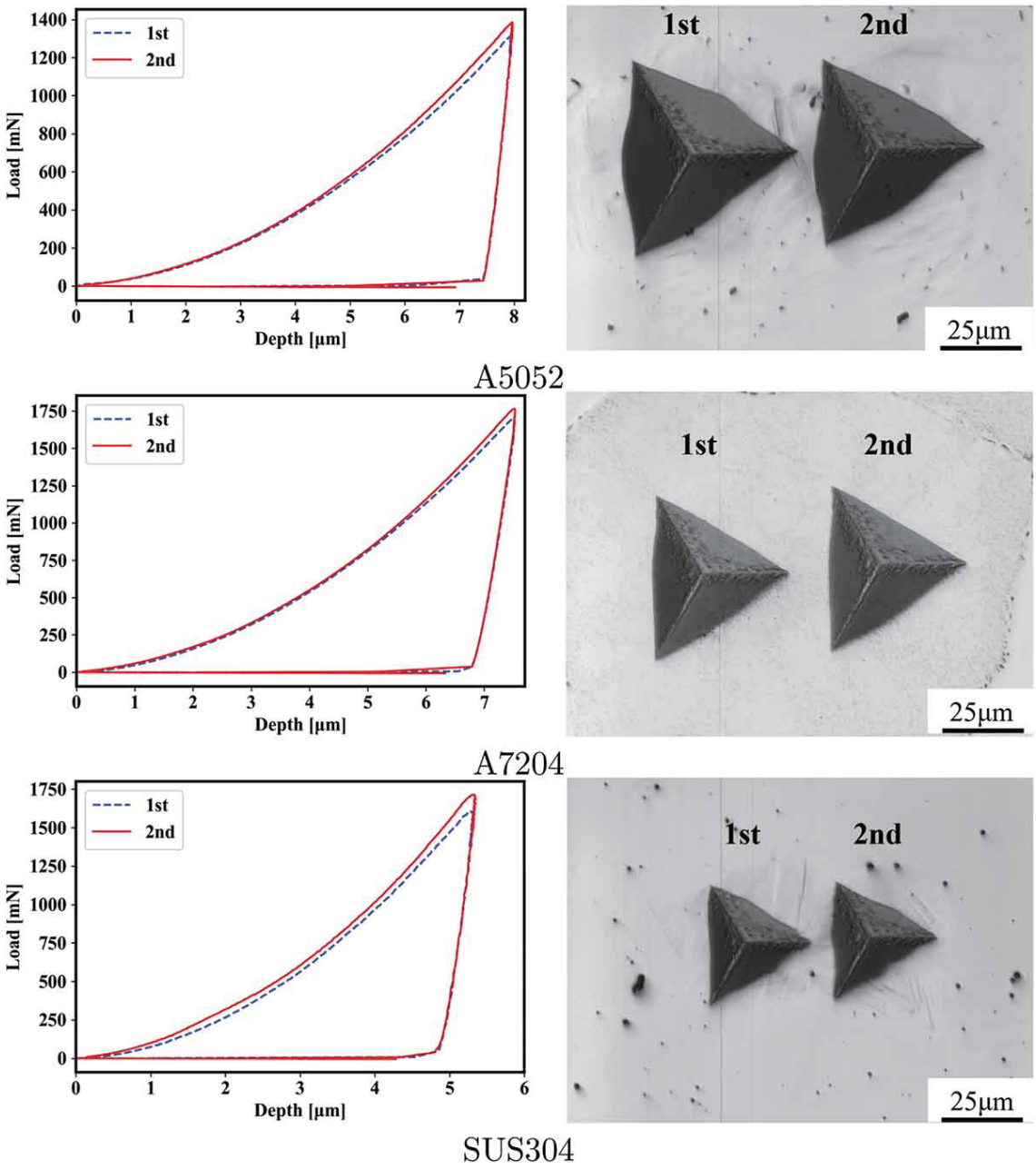

Fig. 3.4 Experimental results: Load–depth curves and indentation impressions of the neighboring indentation test.

Estimation results using neighboring indentation test

The experimental values are presented with two curves in **Fig. 3.1** and **Fig. 3.2**. The intersection point indicated by a rhomboid mark is the corresponding material constant. Plastic properties were determined from the set of the two figures, as shown in **Table 3.7**. The stress-strain curves of the experimental data and estimation results including the previous approach in section 3.3.1 are shown in **Fig. 3.5**. These results agree with the experimental results, especially in aluminum alloys. The estimated and experimental yield stress and ultimate tensile strength of the three samples are calculated and listed in **Table 3.8**. Although the yield stress shows a higher difference between the estimated and experimental results, the ultimate tensile strength shows better accuracy in all three samples. It may be caused by the large equivalent plastic strain beneath the indenter, the estimated plastic properties are closer to the real stress-strain relationship at finite strain region. The previous approach shows a more accurate estimation in yield stress, which is due to the indentation parameters we chose to estimate the plastic properties in this neighboring indentation method. In the neighboring indentation method, the curvature difference between two indentations at the neighboring position represented the work-hardening nature during the indentation, which is more sensitive to the plastic properties at finite strain region rather than yield behavior. The power-law hardening used in this study cannot follow the linear hardening behavior shown in **Fig. 3.5** (b). Even so, the outline of the stress–strain curve is reproduced particularly in the finite strain region. As described above, the neighboring indentation method was validated. In this approach, by obtaining the load curvatures C_1 and C_2 under the above-mentioned conditions, the stress-strain curve could be estimated from the response surfaces shown in **Fig. 3.1** and **Fig. 3.2** in aluminum alloys and steels.

Table 3.7 Material constants estimated by the neighboring indentation method.

Material	σ_0 [MPa]	n
A5052 aluminum	142.3	0.187
A7204 aluminum	338.3	0.08
SUS304 stainless steel	317.3	0.215

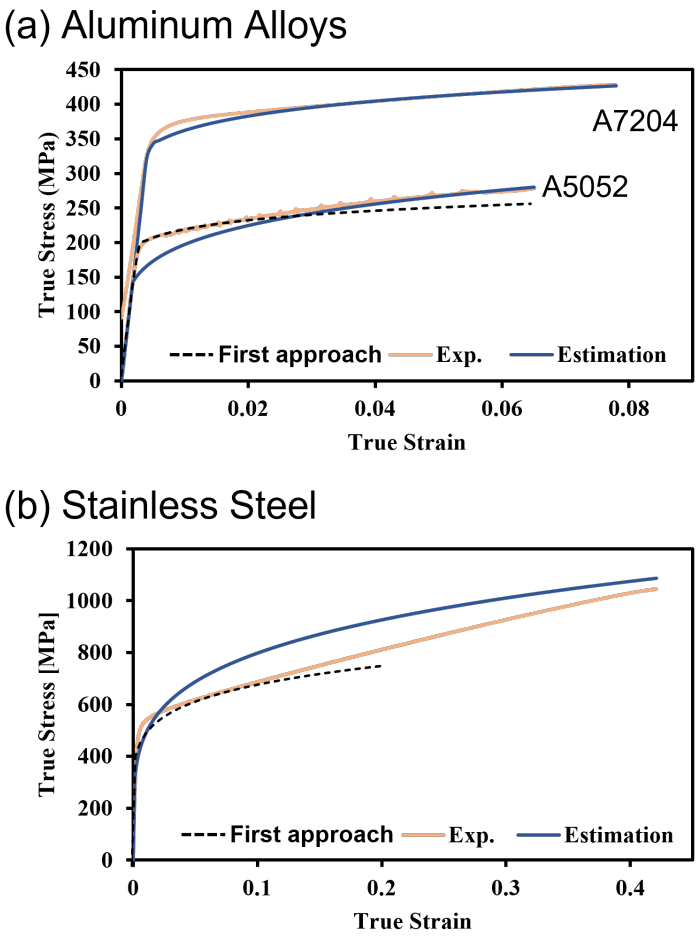

Fig. 3.5 Stress–strain curves estimated by the neighboring indentation method.

Table 3.8 The yield stress and ultimate tensile strength of estimation and experimental stress-strain curves.

Material	Exp.		Est.		Difference	
	YS [MPa]	UTS [MPa]	YS [MPa]	UTS [MPa]	YS [%]	UTS [%]
A5052	205.81	261.55	165.97	261.82	19.43	0.05
A7204	345.33	395.95	341.09	394.99	1.23	0.24
SUS304	485.56	691.08	411.36	729.8	15.36	5.62

3.3.3 Estimation using modified constitutive model

Experimental parameters

The Instrumented indentation tests were performed with TI950 TriboIndener (Bruker, USA) high-load module using a Berkovich indenter. The SUS304 stainless steel sample surface was prepared by mechanical polishing followed by electrical polishing to remove the residual plastic strains. The displacement-control mode was used as a simulation condition. The maximum indentation depth h_{max} was defined as 5.3 μm due to the load limit of the equipment. The loading and unloading rates were set as 0.1 μm/sec. The instrumented indentation tests were performed twelve times, and the averaged values were used to reduce experimental errors. The pile-up topography of the indentation impression was measured by the scanning probe microscope in TI950 TriboIndener.

Experimental results

The load-depth curve and indentation impression of SUS304 stainless steel is shown in **Fig. 3.6**. The curvature C of the loading curve and the pile-up height Z_{max} of indentation impression were calculated from the experimental results; the average value and deviations of the twelve indentation tests are shown in **Table 3.9**. From these results, the material constants in the constitutive model were determined in section3.3.3.

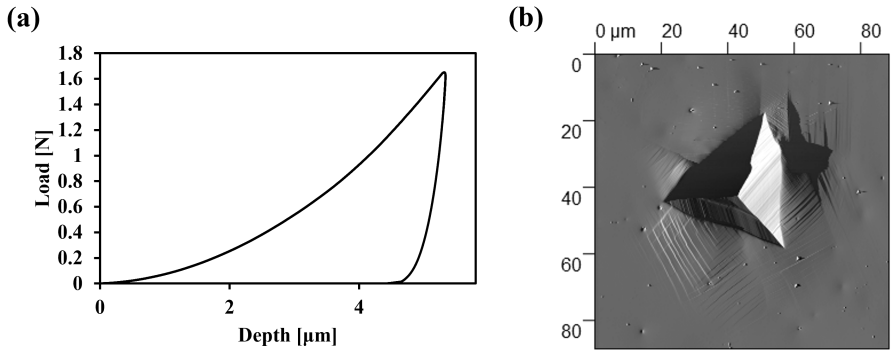

Fig. 3.6 Experimental results: (a) load-depth curve, (b) scanning probe microscope image of indentation impression.

Table 3.9 Averaged loading curvatures, pile-up heights, and the deviations obtained from twelve indentation tests.

Material	C [GPa]	Z_{max}/h_{max}
SUS304 stainless steel	57.63±2.31	0.155±0.025

Determination of material constants

First, the response surface of indentation parameters using linear ($n = 0$) and power-law hardening ($H_p = 0$) model was estimated by finite element simulations. The material constants in both models were determined based on the experimental results of the indentation test shown in the previous section. After that, the critical plastic strain ξ^{cr} and critical linear hardening coefficient H_p^{cr} were defined by the estimation results at both models. The response surface of indentation parameters at $H_p = H_p^{cr}$ were then extracted from the three-dimensional material database to determine the material constants, and the estimated result was compared with the experimental tensile test.

In case $H_p = 0$

At $H_p = 0$, the constitutive model can be simplified as follows

$$\sigma_Y = \sigma_0^{1-n} \left(\sigma_Y + E^* \xi\right)^n , \tag{3.1}$$

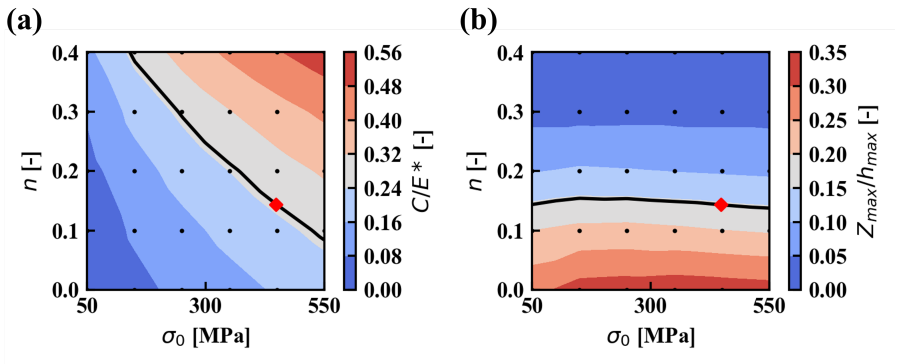

Fig. 3.7 Response surface of (a) normalized loading curvature, (b) normalized pile-up height of indentation impression at $H_p = 0$.

which is the power-law hardening model.The response variables C/E^* and Z_{max}/h_{max} were calculated in the range of $\sigma_0 \in [50\text{MPa}, 550\text{MPa}]$ and $n \in [0.0, 0.4]$ for Young's modulus $E = 200\text{GPa}$. The distributions of the response variables at $H_p = 0$ are shown in **Fig. 3.7**. Based on the calculated mesh data (6×5), the response surfaces were drawn with a bilinear interpolation function. The calculated points were indicated by dots in **Fig. 3.7**. The experimental values are presented with two curves in **Fig. 3.7**, and the intersection point indicated by a rhomboid mark is the corresponding material constant.

In case $n = 0$

At $n = 0$, the constitutive model can be simplified as follows

$$\sigma_Y = \sigma_0 + H_p \xi, \tag{3.2}$$

which is the linear hardening model.The response surface of C/E^* and Z_{max}/h_{max} calculated in the range of $\sigma_0 \in [50\text{MPa}, 650\text{MPa}]$ and $H_p \in [0, 2500]$ for Young's modulus $E = 200\text{GPa}$ are shown in **Fig. 3.8**. The experimental values are presented with two curves in **Fig. 3.8**, and a rhomboid mark indicates the intersection point is the corresponding material constant. The estimated material constants and corresponding plastic properties at $H_p = 0$ and $n = 0$ are shown in **Table 3.10** and **Fig. 3.9** (b). By considering both simple constitutive models, the

Table 3.10 The estimated material constants at each case.

Cases	σ_0 [MPa]	n	H_p
$H_p = 0$	447.45	0.1433	0
$n = 0$	582.93	0	1295.3
$H_p = H_p^{cr}$	540.9	0.0444	915.78

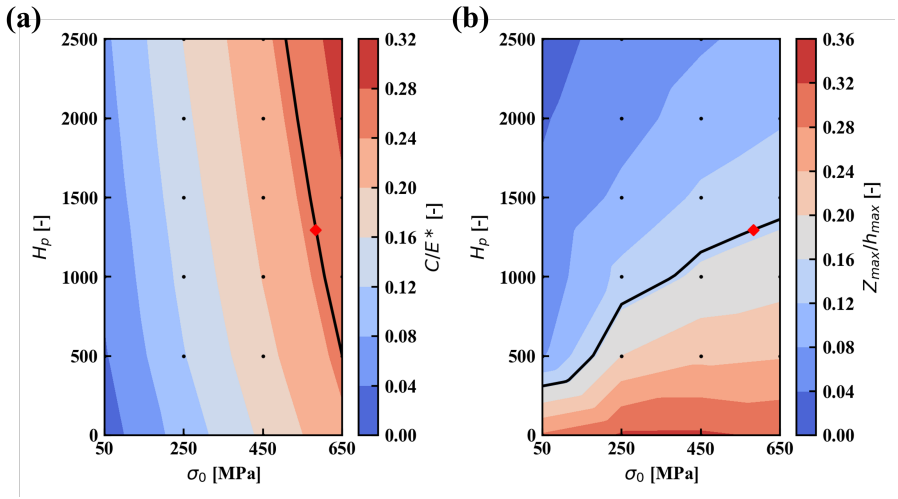

Fig. 3.8 Response surface of (a) normalized loading curvature, (b) normalized pile-up height of indentation impression at $n = 0$.

deformation behavior of real alloy should lay between the linear and power-law hardening curves as in **Fig. 3.9** (a). The estimated results should be adjusted between the linear and power-law hardening curves to get more accurate estimation results.

Determination of ξ_{cr} and H_p^{cr}

To adjust the estimation results between two hardening models, the material constants at $H_p = 0$ and $n = 0$ were used to determine the critical plastic strain ξ_{cr}. The material constants at $H_p = 0$ and $n = 0$ were determined from the same indentation parameters, which means this deformation behavior of estimated results should be identical at a specific plastic strain state ξ^{cr}. From the estimation results of two hardening models, we define the plastic strain of the intersection point between two curves as ξ^{cr}, the linear hardening coefficient of linear

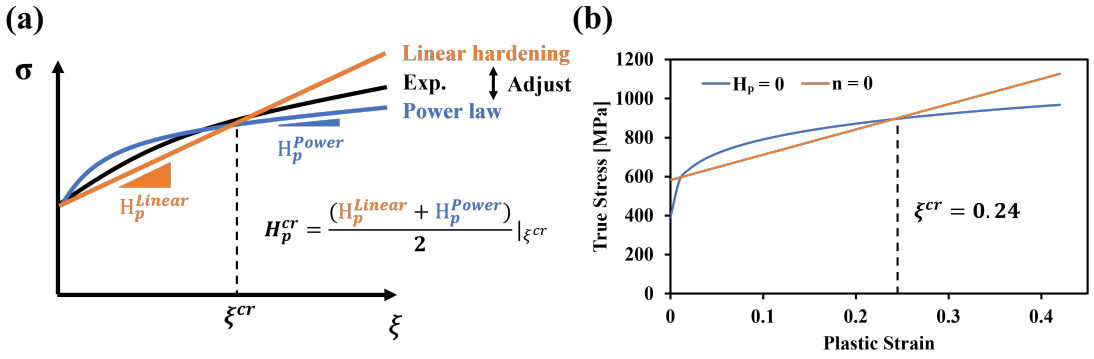

Fig. 3.9 Stress-strain curves estimated by instrumented indentation test: (a) schematic diagram and (b) estimated results at $H_p = 0$ and $n = 0$.

hardening model H_p^{Linear} and power-law hardening model H_p^{Power} are defined as

$$H_p = \frac{\partial \sigma^*}{\partial \xi}|_{\xi_{cr}}, \tag{3.3}$$

and the critical linear hardening coefficient H_p^{cr} is defined as follows

$$H_p^{cr} = \frac{H_p^{Linear} + H_p^{Power}}{2}|_{\xi^{cr}}. \tag{3.4}$$

From **Fig. 3.9** (b), the critical plastic strain was determined as $\xi^{cr} = 0.24$ and the corresponding critical linear hardening coefficient $H_p^{cr} = 915.78$.

Determination of material constants

From the three-dimensional material database shown in **Fig. 3.10** (a), the response surface in the range of $\sigma_0 \in [50\text{MPa}, 650\text{MPa}]$ and $n \in [0.0, 0.4]$ at $H_p^{cr} = 915.8$ can be extracted and shown in **Fig. 3.10** (b) and (c). The experimental values are presented with two curves in **Fig. 3.10**, and the intersection point indicated by a rhomboid mark is the corresponding material constants shown in **Table 3.10**.

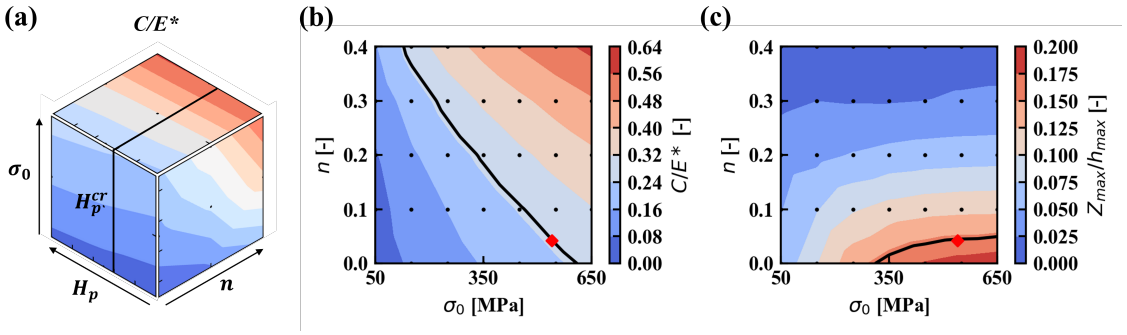

Fig. 3.10 Response surface of (a) normalized loading curvature, (b) normalized pile-up height of indentation impression at $H_p = H_p^{cr}$.

Estimation results using a modified constitutive model

The stress-strain curves of the experimental data and estimation results, including the previous approach[63], are shown in **Fig. 3.11**. The estimation results combining the linear and power-law hardening model agree with experimental results, and the estimated hardening behavior is more consistent than the previous approaches using the simple power-law constitutive model. The calculated yield stress and ultimate tensile strength are shown in **Table 3.11**. In this new estimation method, both the yield stress and the ultimate tensile strength show more precise estimation compared with the previous approach, which shows the estimation accuracy is hugely affected by the constitutive model. And the modified constitutive model used in this method shows good expressiveness for the plastic properties of high work-hardening alloy.

Table 3.11 The yield stress and ultimate tensile strength of estimation and experimental stress-strain curves.

Material	Exp.		Est.		Difference	
	YS [MPa]	UTS [MPa]	YS [MPa]	UTS [MPa]	YS [%]	UTS [%]
Power-law hardening model	485.56	691.08	411.36	729.8	15.36	5.62
Modified constitutive model	**485.56**	**691.08**	**559.57**	**701.8**	**5.44**	**1.56**

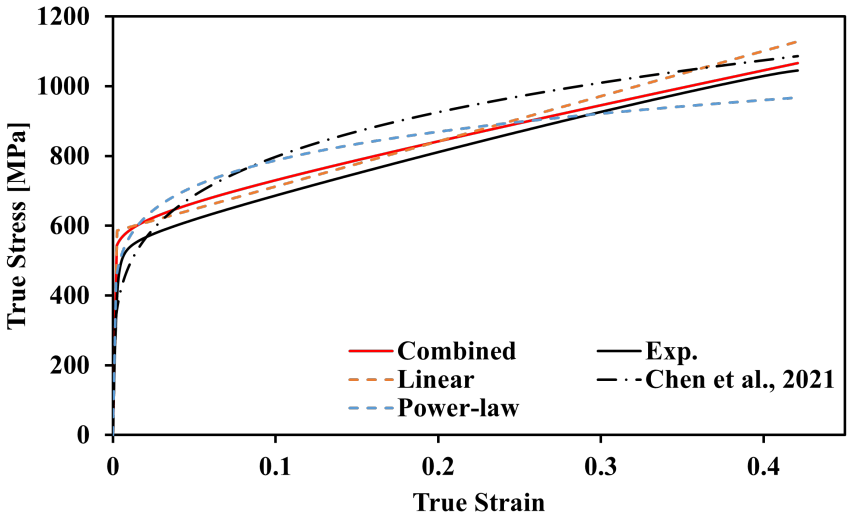

Fig. 3.11 Stress-strain curves estimated by instrumented indentation test at H_p^{cr}.

3.4 Summary

In this chapter, the estimation methods of plastic properties purposed by this study were validated for application to aluminum alloys and a stainless steel. The experimental parameters determined in chapter 2, C_1, Z_{max}/h_{max}, and $(C_2 - C_1)$, were used to estimate the material constants using instrumented indentation. Estimation results based on a single indentation with pile-up topography shows good agreement with experimental tensile results. Compare with the existing estimation method, dual indenter technique, this approach provide similar estimation results but less experimental requirement.

Based on the neighboring indentation method, a material database comprising two response surfaces for two material constants of a plastic constitutive model was developed for aluminum alloys and steels using numerical simulations based on the finite element method. Using the database, a set of material constants can be determined easily. The produced database was validated by comparison with the corresponding experiments. These results agree with the experimental results, especially in aluminum alloys. The power-law hardening used in this study cannot follow the linear hardening behavior shown in **Fig. 3.5** (b). To estimate the linear hardening behavior, a new estimation method using modified constitutive model

was proposed. The estimation results agrees with the experimental tensile test and represent the hardening behavior more accurate than previous approaches.

Following the proposed concept, a material database can be generated for various alloys with different Young's moduli. Those approaches are practical because the experiment can be performed using a single standard sharp indenter, and computational simulations can be performed in advance. In addition, it is applicable to high-throughput experiments.

Chapter 4

Estimation of strain-rate-dependent plastic properties

4.1 Introduction

In previous chapter, the estimation method at room temperature is based on the rate-independent constitutive model. In this chapter, we developed an approach for estimation of strain-rate-dependent plasticity based on the results of the high-temperature indentation tests. Initially, the simple constitutive model used in previous approaches was extended to a strain-rate-dependent format. Next, high-temperature indentation tests were performed under different loading rates for an aluminum alloy specimen. Subsequently, the material constants of the proposed constitutive model were determined to minimize the difference between the experimental *P–h* curves and the curves obtained from their corresponding finite element simulations. Lastly, the estimated mechanical properties were validated using a compression test at the same temperature.

4.2 Finite element modeling

The constitutive model in a strain-rate-dependent form was introduced in section 2.2.4 and the finite element model was defined for the following computational simulations of high-temperature indentation tests.

4.2.1 Finite element model of the instrumented indentation test

A three-dimensional finite element model of a specimen and Berkovich indenter was constructed for the computational simulations of the instrumented indentation tests described in Section 4.3.2, as shown in **Fig. 4.1**. A mirror symmetrical boundary condition was applied to the *X*–*Y* plane along the center of the object, and the vertical displacement along the bottom of the finite element model was constrained. The finite element model contains 15,358 nodes and 14,138 eight-node hexahedral elements with reduced integration, in which the contact area between the specimen and indenter was discretized more finely than the other areas. The indenter was assumed to be a rigid body. The friction between the indenter and the sample was not considered in this study because the effect of friction on the indentation results is insignificant in the case of Berkovich indenter [33]. The friction effect was confirmed to be minor in simulations of the instrumented indentation tests using the strain-rate-dependent plasticity. A load was applied to the top of the indenter. Quasi-static boundary value problems were solved using the applied load control with an implicit scheme.

4.2.2 Finite element model of the compression test

An axisymmetric finite element model was constructed for the computational simulations of the compression tests described in Section 4.3.2, as shown in **Fig. 4.2**. The finite element model contained 990 nodes and 940 four-node quadrilateral and 4 three-node triangular axisymmetric elements, where triangular elements were employed for the corners of the specimen to avoid excessive distortion of the elements. The vertical displacement along the bottom of the finite element model was constrained. Coulomb friction model was

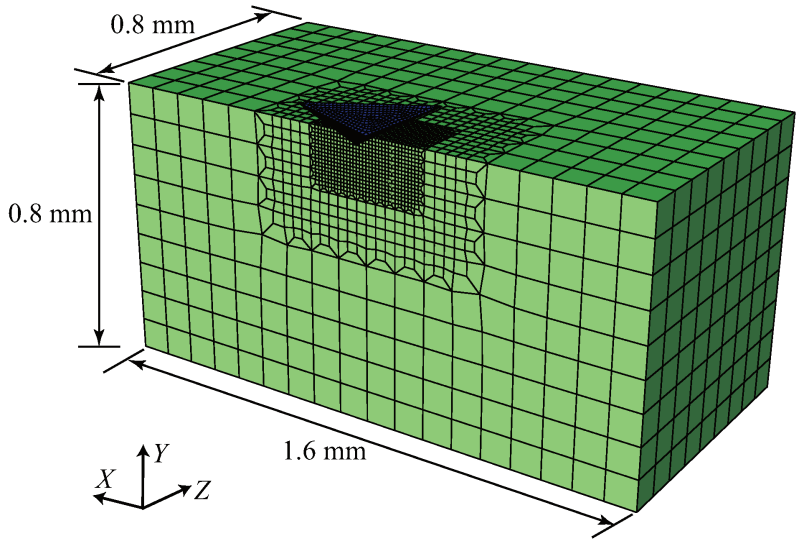

Fig. 4.1 Finite element model of the instrumented indentation test.

employed, and its coefficient was calibrated as 0.16 to reproduce the experimental barreling deformation in the simulations. Simulations were performed using displacement control at the top of the model and solved as quasi-static boundary value problems with an implicit scheme.

4.3 Experiments

Experimental data were acquired to characterize and validate the strain-rate dependency of the plastic properties, where the instrumented indentation and compression tests at high temperature were performed at different test speeds.

4.3.1 Specimen

A wrought aluminum alloy with a grain size of approximately 200 μm was used in this study. The alloy composition is shown in **Table 3.2** with solution heat treatment at 475°C. A melting temperature of a similar alloy (A7204) is 635 °C [64]. For instrumented indentation tests, mechanical polishing with diamond and colloidal silica suspensions was conducted on

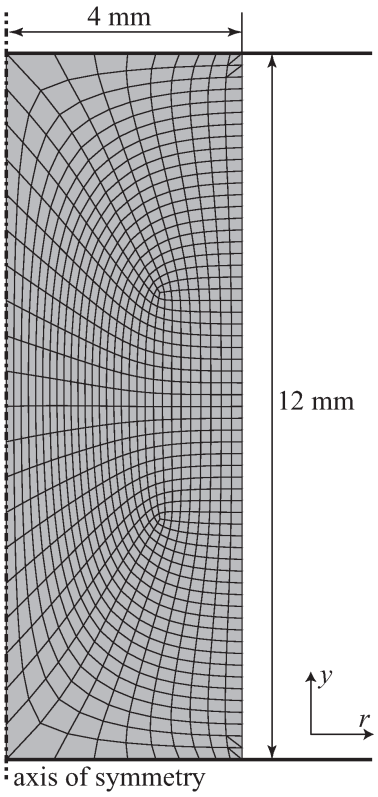

Fig. 4.2 Finite element model of the compression test.

the sample surface, followed by electrical polishing to remove the residual plastic strains. The mechanical polishing condition of aluminum alloy are shown in **Table 3.4**. The material constants of the constitutive model at room temperature were determined under the assumption of an independent strain-rate ($\alpha \approx 0$, $m \approx 0$).

$$(E,\ \nu,\ K_p,\ n) = (70\text{GPa},\ 0.3,\ 353.4\text{MPa},\ 0.08), \tag{4.1}$$

that also can be determined from the instrumented indentation tests in previous chapter [63]. The work-hardening exponent was approximately zero.

4.3.2 Instrumented indentation tests at high temperatures

Instrumented indentation tests were performed at room temperature to 300 °C using a diamond Berkovich indenter with the TI 950 TriboIndenter and xSol High-Temperature Stage (Bruker, Billerica, MA, USA). To prevent the degradation of the specimen surface and indenter tip, the sample surface was protected by an inert argon atmosphere. The following experimental procedure for high-temperature indentation tests was established in our previous study [44]. The indenter tip were passively preheated by approaching sample surface with 100μm gap and hold around 30 minutes for thermal equilibrium at each temperature. After passively preheating the indenter tip at target temperature, the instrumented indentation tests were performed for a maximum applied load of 1.5 N. The applied load was applied with three different load rates, i.e., 0.1, 1.0, and 10 N/s, with the unloading rate set to 0.1 N/s for each case after 10 s holding time at the maximum load. The indentation tests were performed five times for each condition to ensure reproducibility. The impressions of high-temperature indentation tests in loading rates of 0.1 and 10 N/s at 300 °C are shown in **Fig. 4.3**, which were observed with a scanning electron microscopy (JSM-7001F, JEOL Ltd., Tokyo, Japan). According to these figures, the indentation tests were performed without crack, and no significant difference between them was found in the impressions. The $P - h$ curves of aluminum alloy from room temperature to 300 °C are shown in **Fig. 4.4**. At room temperature, the $P - h$ curves shows rate-independent behavior. The rate-dependency increase with increas-

ing temperature, and obvious rate-dependent-plasticity was observed at 300 °C. The $P - h$ curves at 300 °C were used to determine the rate-dependent material constants of aluminum alloy.

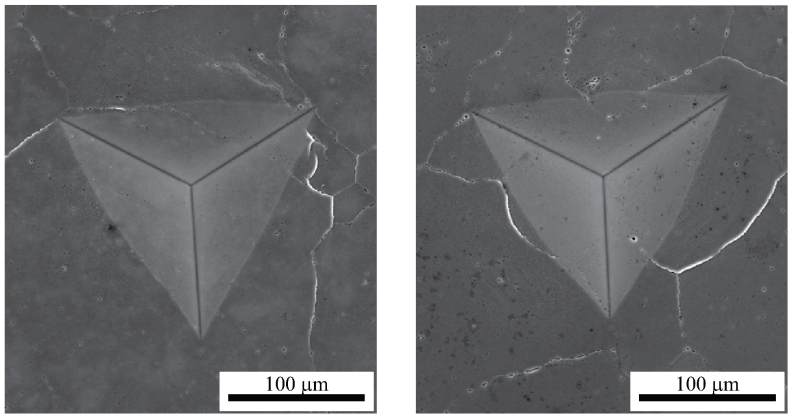

(**a**) 0.1 N/s (**b**) 10 N/s

Fig. 4.3 Impression of high-temperature indentation in loading rates of 0.1 and 10 N/s.

4.3.3 Compression tests at high temperatures

For the validation of the estimated material response, compression tests of the aluminum alloy were performed at three different test speeds (1.20, 0.12, and 0.06 mm/s; 0.10, 0.01, and 0.005/s in strain rate) in a chamber heated at 300 °C. Cylindrical samples (12 mm height, 8 mm diameter) corresponding to **Fig. 4.2** were compressed in the axial direction under displacement control using a precision Autograph AG-X Series universal tester (Shimadzu, Kyoto, Japan). The sample surface was lubricated to minimize bulging deformation in these tests. The aluminum samples after high temperature compression test were shown in **Fig. 4.5**.

4.4 Characterization of strain rate dependency

In this section, material constants of the strain-rate-dependent plasticity were determined to minimize the difference between experiments and its computational simulations in high-

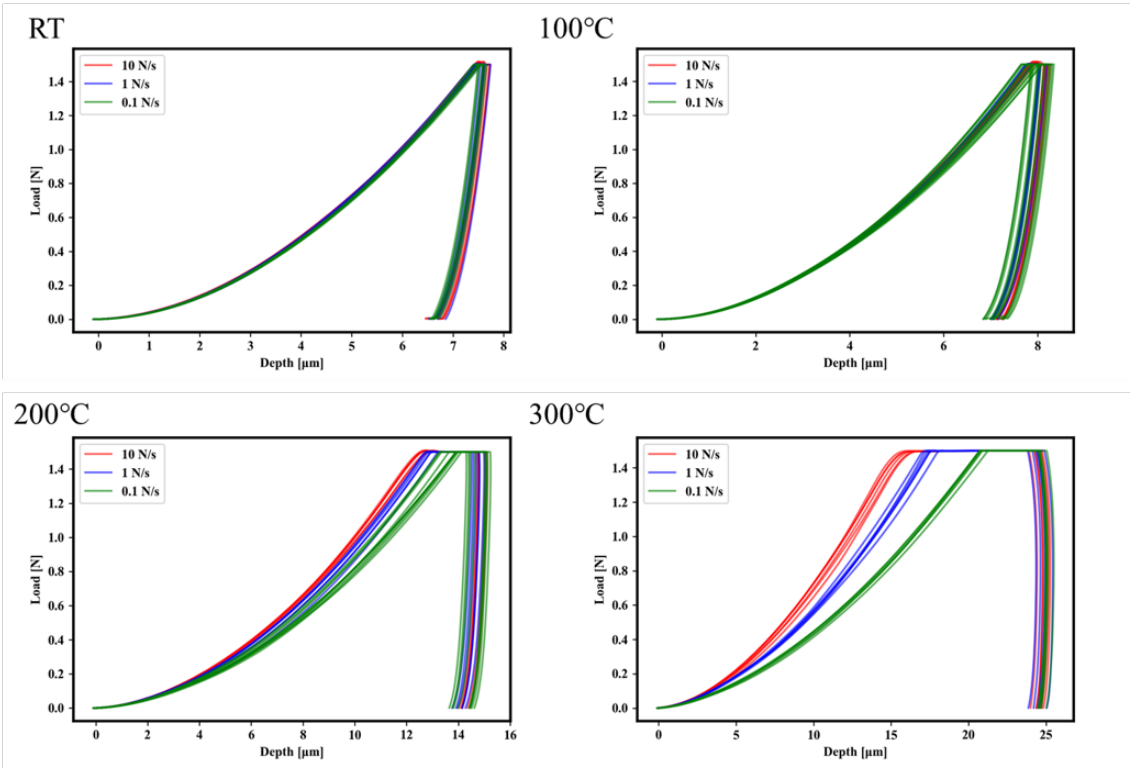

Fig. 4.4 The $P-h$ curves of aluminum alloy at room temperature to 300°C with different load rates.

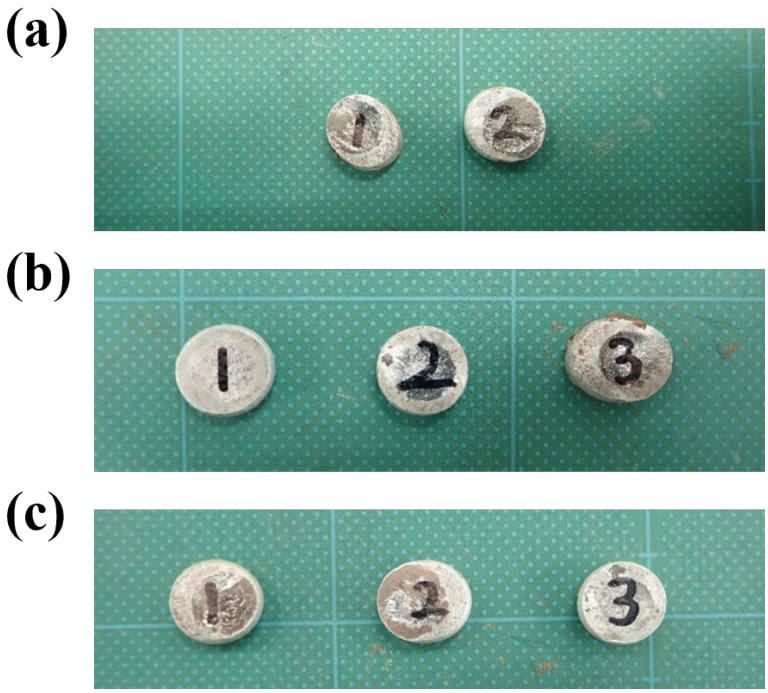

Fig. 4.5 The aluminum samples after high temperature compression test at 300°C with different test speeds (a) 1.2mm/s (b) 0.12mm/s (c) 0.06mm/s.

temperature indentation tests. Moreover, the material response based on the constitutive model and the determined material constants was validated in compression tests at the same temperature.

4.4.1 Determination of material constants

The material constants were determined to minimize the difference in the P–h curves between the experiments and the corresponding simulations for three loading speeds. In this study, the elastic constants E and n at 300 °C were obtained from the literature [65] as 59 GPa and 0.35, respectively. The work-hardening exponent n was assumed to be 0.08, which is considered identical to that of the tensile test at room temperature for simplicity. Thus, the optimization problem is defined as follows:

$$\begin{aligned} &\text{minimize}[\Delta(K_p, K_{vp}, m)], \\ \Delta := &\sum_{i=1}^{N_{case}} \left\{ \frac{1}{h_i^{\text{exp,eh}}} \left(|h_i^{\text{exp,bh}} - h_i^{\text{sim,bh}}| + |h_i^{\text{exp,eh}} - h_i^{\text{sim,eh}}| \right) \right\}, \end{aligned} \tag{4.2}$$

where $h_i^{\text{exp,bh}}$, $h_i^{\text{sim,bh}}$, $h_i^{\text{exp,eh}}$, and $h_i^{\text{sim,eh}}$ are the indentation depths at the beginning and end of the holding process in the experimental and simulation results of the i-th case, respectively. N_{case} is the number of the loading rate cases. In this study, $N_{case} = 3$, as specified in Section 4.3.2. Δ is the difference between the experimental and simulated P–h curves. In the both cases of $\alpha \in (0, 1)$ and $\alpha = 1$, the sets of material constants were determined to solve the optimization problem (Equation (4.2)) using the Levenberg–Marquardt method [61] as follows:

$$\begin{aligned} \alpha \in (1, 0) : (K_p, K_{vp}, m) &= (17.4\text{MPa}, 115.5\text{MPa}, 0.2367), \\ \alpha = 1 : (K_{vp}, m) &= (120.0\text{MPa}, 0.160) \end{aligned} \tag{4.3}$$

where Δ was 0.0731 for $\alpha \in (0, 1)$ and 0.0784 for $\alpha = 1$. For $\alpha \in (0, 1)$, the strain-rate-independent- initial yield strength is calculated as $\sigma_Y = 8.48$ MPa. Although the strength

is non-negligible, the appropriate material constants can be found even in the case of $\alpha = 1$ (under the constraint of $K_p \equiv 0$). The P–h curves obtained in the experiments and simulations using the determined material constants are shown in **Fig. 4.6**. Additionally, the relationship between the depth and time during the holding process at the maximum applied load is shown in **Fig. 4.7**. The strain-rate-dependent deformation behavior in the instrumented indentation tests was reproduced in computational simulations using the constitutive model in both cases. But the unloading part shows a difference between the simulation and experiment. The unloading curves in the experiment show the creep behavior still occurs even in the unloading stage, which caused the curvature shape in unloading curves. The creep behavior in the unloading stage cannot be well represented by the simulation, which may be due to the experimental condition or the limitation of the constitutive model. From the results of the finite element analyses in the case of $\alpha \in (0, 1)$, the distributions of Mises stress and equivalent plastic strain at the beginning and end of the holding processes for the loading rates of 0.1 and 10 N/s are shown in **Fig. 4.8** and **Fig. 4.9**, respectively. At the beginning of the holding process at the maximum applied load, the stress concentration around the indenter tip was observed in the case of a high loading rate, whereas the stress distribution was uniform in the case of a slow-loading rate due to the relaxation provided by the strain-rate-dependent deformation during the loading process. In addition, the distributions of an equivalent plastic strain before and after the holding process exhibit the evolution of the equivalent plastic strain during the holding process, which is more prominent in the case of a high loading rate.

4.4.2 Validation in compression tests

Using the constitutive model (Equation (2.37)) and determined material constants (Equation (4.3)), computational simulations of the compression tests at three test speeds (1.20, 0.12, and 0.06 mm/s) were performed. The friction coefficient 0.16 of the compression tests simulation was determined by the surface morphology of the samples after compression tests and simulations shown in **Fig. 4.10**.

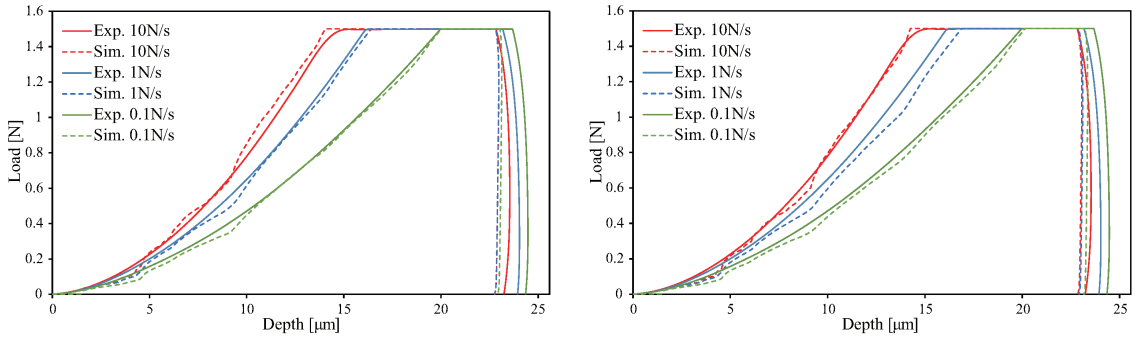

(**a**) $\alpha \in (0,1)$ (**b**) $\alpha = 1$

Fig. 4.6 Load–depth curves obtained in the experiments and simulations using the determined material constants. The dashed lines indicate the simulation results.

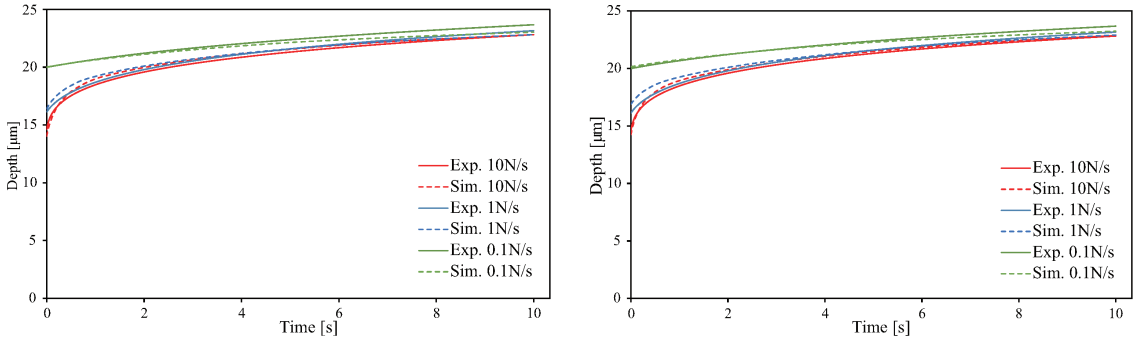

(**a**) $\alpha \in (0,1)$ (**b**) $\alpha = 1$

Fig. 4.7 Depth–time curves obtained in the experiments and simulations using the determined material constants. The dashed lines indicate the simulation results.

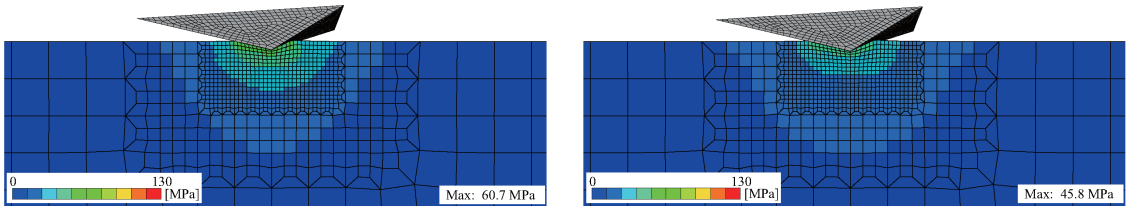

(**a1**) Beginning of holding (**a2**) End of holding

(**a**) 0.1 N/s

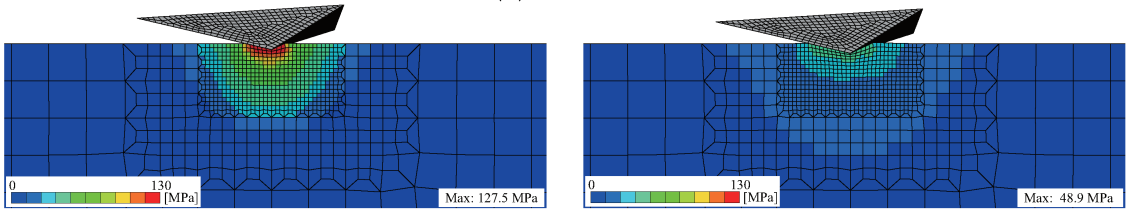

(**b1**) Beginning of holding (**b2**) End of holding

(**b**) 10 N/s

Fig. 4.8 von Mises stress distribution at the beginning and end of the holding processes in the computational simulations using the determined material constants for $\alpha \in (0, 1)$.

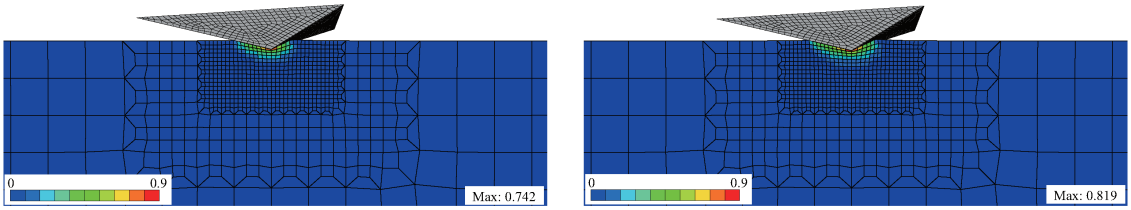

(**a1**) Beginning of holding (**a2**) End of holding

(**a**) 0.1 N/s

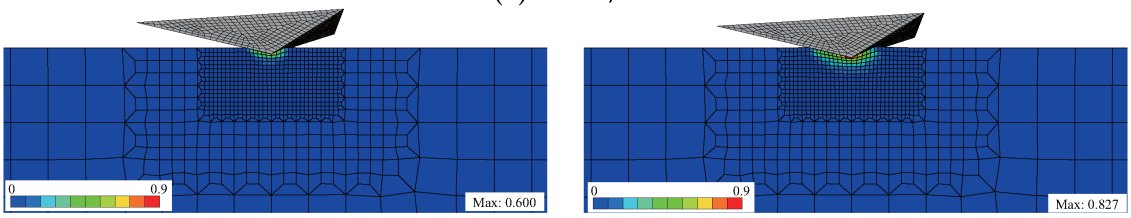

(**b1**) Beginning of holding (**b2**) End of holding

(**b**) 10 N/s

Fig. 4.9 Equivalent plastic strain distribution at the beginning and end of the holding processes in the computational simulations using the determined material constants for $\alpha \in (0, 1)$.

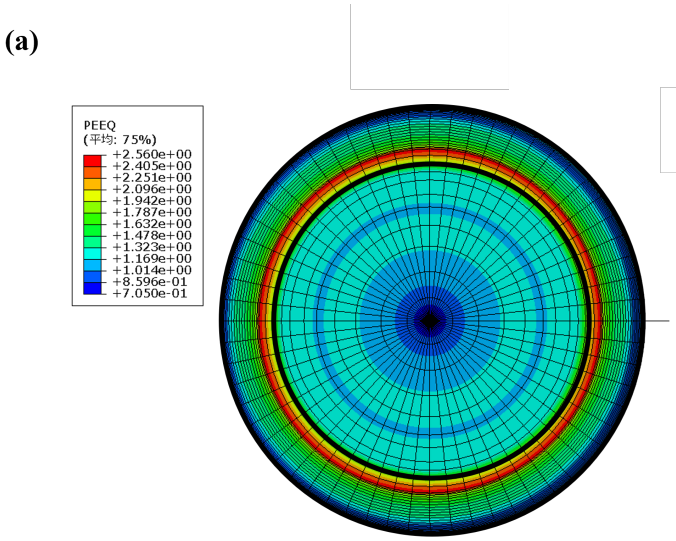

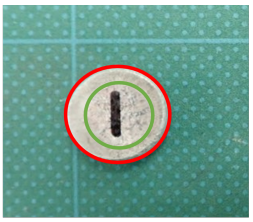

(c)

Friction coefficient	Area ratio (%)
0.05	88.7
0.075	81.4
0.1	70.6
0.15	57.3
0.16	52.65
0.18	48.74

Fig. 4.10 (a) The surface morphology of compression test simulations and (b) the samples after compression tests (c) the relationship of friction coefficient and area ratio.

The load–stroke curves obtained from the experiments and simulations at 300 °C are shown in **Fig. 4.11**. The results indicate that the load levels of the simulations are less consistent than those of the experiments, although the strain-rate-dependent material responses were characterized in the computational simulations. In other words, the constitutive model is applicable for reproducing the material behavior at high temperature; however, the material responses evaluated in the instrumented indentation tests did not agree with those obtained in the compression tests.

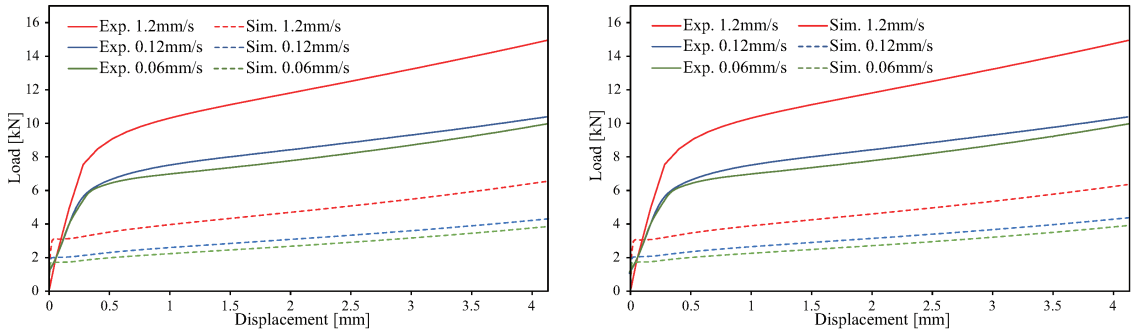

(**a**) $\alpha \in (0, 1)$ (**b**) $\alpha = 1$

Fig. 4.11 Load–stroke curves in the experiments and simulations using the determined material constants. The dashed lines indicate the simulation results.

The critical difference between the instrumented indentation test and bulk test is the scale of the deformation domain. In the instrumented indentation tests, the influence region of the residual stress and plastic deformation is estimated as smaller than a hemisphere with a radius of 500 μm as shown in **Fig. 4.8** and **Fig. 4.9**; i.e., the evaluation domain contained a few crystal grains. Therefore, the instrumented indentation tests were not carried out for a polycrystal. This can be considered as an origin of the discrepancy. In fact, distinctive material behaviors at high temperature such as grain boundary sliding were reported in aluminum alloys [66),67)]. The microscopic heterogeneity does not have a significant effect at room temperature [1),68),63)]; however, the discrepancy arises particularly at high temperature. The scale and temperature effects require further investigations.

4.5 Summary

A new estimation approach for strain-rate-dependent plasticity was developed based on the instrumented indentation tests, where the material constants of the strain-rate-dependent constitutive model were determined from the results of experiments and the corresponding computational simulations at different test speeds. This approach can estimate the strain-rate-dependency of the material response in high-temperature indentation tests; however, the estimated mechanical properties were not consistent with the results of the compression tests. The estimation of bulk properties using high-temperature indentation tests remain an unsolved problem.

In this study, we focused on the material behavior of one alloy sample under the isothermal single condition. Through a systematic examination of various samples and thermal conditions, the microstructure and temperature dependencies can also be characterized using the proposed approach.

Chapter 5

Conclusions

In Chapter 1, the brief introduction of the mechanical properties of alloys and the instrumented indentation test has been discussed. Compared with the standard tensile/compression test, instrumented indentation test shows excellent potential for the high-throughput evaluation for the mechanical properties. The existing approaches using instrumented indentation test to estimate the stress-strain relationship corresponding to the tensile test show some experiment limitation and accuracy problems. To solve these problems, the purpose of this thesis is to propose a new estimation method of plastic properties using instrumented indentation test with a single indenter.

In Chapter 2, the estimation method of plastic properties using instrumented indentation test has been discussed in detail. Following the basic theory of metal plasticity, the strain-rate independent and dependent constitutive model used in this study has been proposed to represent the plastic properties of alloys. In this chapter, two different estimation methods were proposed to estimate the plastic properties of alloys using instrumented indentation tests. First, the sensitivity of experimental parameters from a single indentation test result was numerically examined. The pile-up height and curvature of the loading part of the p-h curve were used to determine the material constants of the constitutive model. The finite element model and the solution method used in this study have also been introduced in this chapter. Second, the neighboring indentation test was proposed to estimate the plastic

properties by utilizing the interaction between the two indentations at neighboring positions. The neighboring indentation method's suitable experimental parameters and conditions were numerically examined. The curvature difference between the two indentations was used to determine the material constants of the constitutive model. The next chapter will validate the proposed methods for application to aluminum alloys and stainless steel.

In Chapter 3. Firstly, the estimation results using pile-up height and loading curvature of the $P - h$ curve show good agreement with experimental tensile results and existing approaches. The neighboring indentation test was also used to determine the material constants that show more accurate estimation results than only considering the single $P - h$ curve and pile-up height. But the linear hardening behavior of stainless steel cannot be represented by a simple power-law hardening model; a new estimation method with the modified constitutive model was proposed to improve the accuracy of the estimation results. The modified constitutive model and the estimation method's detail have been discussed and show better estimation results in yield stress and ultimate tensile strength.

In Chapter 4, the above approaches only consider strain-rate-independent plasticity. To extend this estimation method to rate-dependent plasticity, the high temperature instrumented indentation results with different loading rates were used to determine the material constant of a modified rate-dependent constitutive model. This method was validated to aluminum alloy at 300 °C, and the estimated material constants were compared with the compression test at the same temperature. Although the modified constitutive model can represent the rate-dependency of instrumented indentation results, the load level of the simulation is less consistent than those of the experiments. However, the strain-rate-dependent material responses were characterized in the computational simulations. In other words, the constitutive model is applicable for reproducing the material behavior at high temperatures; however, the material responses evaluated in the instrumented indentation tests did not agree with those obtained in the compression tests. The critical difference between the instrumented indentation test and the bulk test is the scale of the deformation domain. Specific material behaviors at high temperatures such as grain boundary sliding or local softening were reported in aluminum alloys. The microscopic heterogeneity does not have a significant effect at room

temperature; however, the discrepancy arises particularly at high temperatures. The scale and temperature effects require further investigations.

In summary, the estimation methods of plastic properties using instrumented indentation tests were proposed in this thesis. The suitable experimental parameters and indentation conditions were experimentally and numerically examined. The proposed methods were validated for application to aluminum alloys and stainless steel and showed good agreement compared with the experimental tensile test results. These estimation methods are suitable for high-throughput experiments due to the simple experimental conditions, and the data-driven method can be used for various alloys with different deformation behavior. These approaches can also be extended to characterize the strain-rate-dependent plasticity by combining with the high-temperature indentation test. The high-temperature indentation test results with different loading rates were used to determine the material constants in the strain-rate-dependent constitutive model. The proposed method can characterize the strain-rate-dependency in the high-temperature indentation, but the difference in the load level caused by scale effects remains unsolved. This thesis shows the great potential of instrumented indentation tests as a high-throughput evaluation method of mechanical properties. It is also suitable to characterize the heterogeneous properties in multi-scale. These methods can be further extended by combining with the crystal plasticity finite element method to characterize the transformation- / twinning- induced plasticity and the anisotropy of crystals.

References

1) K. Goto, I. Watanabe, and T. Ohmura, "Determining suitable parameters for inverse estimation of plastic properties based on indentation marks," *International Journal of Plasticity*, vol. 116, pp. 81–90, 2019.

2) J. Ruzic, S. Emura, X. Ji, and I. Watanabe, "Mo segregation and distribution in ti–mo alloy investigated using nanoindentation," *Materials Science and Engineering: A*, vol. 718, pp. 48–55, 2018.

3) I. Watanabe, Z. Sun, H. Kitano, and K. Goto, "Multiscale analysis of mechanical behavior of multilayer steel structures fabricated by wire and arc additive manufacturing," *Science and Technology of Advanced Materials*, vol. 21, no. 1, pp. 461–470, 2020.

4) J. Ruzic, K. Goto, I. Watanabe, T. Osada, L. Wu, and T. Ohmura, "Temperature-dependent deformation behavior of γ and γ' single-phase nickel-based superalloys," *Materials Science and Engineering: A*, vol. 818, p. 141439, 2021.

5) T. Matsuno, R. Ando, N. Yamashita, H. Yokota, K. Goto, and I. Watanabe, "Analysis of preliminary local hardening close to the ferrite–martensite interface in dual-phase steel by a combination of finite element simulation and nanoindentation test," *International Journal of Mechanical Sciences*, vol. 180, p. 105663, 2020.

6) E. D. Hintsala, U. Hangen, and D. D. Stauffer, "High-throughput nanoindentation for statistical and spatial property determination," *Jom*, vol. 70, no. 4, pp. 494–503, 2018.

7) Y. Chen, E. Hintsala, N. Li, B. R. Becker, J. Y. Cheng, B. Nowakowski, J. Weaver, D. Stauffer, and N. A. Mara, "High-throughput nanomechanical screening of phase-

specific and temperature-dependent hardness in al x fecrnimn high-entropy alloys," *JOM*, vol. 71, no. 10, pp. 3368–3377, 2019.

8) A. Ikeda, K. Goto, T. Osada, I. Watanabe, and K. Kawagishi, "High-throughput mapping method for mechanical properties, oxidation resistance, and phase stability in ni-based superalloys using composition-graded unidirectional solidified alloys," *Scripta Materialia*, vol. 193, pp. 91–96, 2021.

9) M. R. VanLandingham, "Review of instrumented indentation," *Journal of Research of the National Institute of Standards and Technology*, vol. 108, no. 4, p. 249, 2003.

10) W. C. Oliver and G. M. Pharr, "An improved technique for determining hardness and elastic modulus using load and displacement sensing indentation experiments," *Journal of materials research*, vol. 7, no. 6, pp. 1564–1583, 1992.

11) J. H. Hollomon, "Tensile deformation," *Aime Trans*, vol. 12, no. 4, pp. 1–22, 1945.

12) P. Ludwik, "Die kegelprobe," in *Die Kegelprobe*, pp. 3–17, Springer, 1908.

13) F. Mohs, *Versuch einer Elementar-Methode zur naturhistorischen Bestimmung und Erkennung der Foßilien*, vol. 1. Gamesinaschen Buhhandlung, 1812.

14) W. Wade, "Hardness of metals," *Reports on experiments on the strength and other properties of metals for cannon with a description of the machines for testing metals, and of the classification of cannon in service*, pp. 259–275, 1856.

15) J. Brinell, "Method of determining hardness and other properties of iron and steel," in *II Congres International des Methodes d'Essai, Paris*, p. 243, 1900.

16) E. Meyer and Z. Ver, "Contribution to the knowledge of hardness and hardness testing," *Zeitschrift Des Vereines Deutscher Ingenieure*, vol. 52, pp. 740–835, 1908.

17) R. L. Smith and G. Sandly, "An accurate method of determining the hardness of metals, with particular reference to those of a high degree of hardness," *Proceedings of the Institution of Mechanical Engineers*, vol. 102, no. 1, pp. 623–641, 1922.

18) F. Knoop, C. G. Peters, and W. B. Emerson, "A sensitive pyramidal-diamond tool for indentation measurements," *Journal of Research of the National Bureau of standards*, vol. 23, no. 1, p. 39, 1939.

19) I. 14577, "Metallic materials – instrumented indentation test for hardness and materials para-meters.," standard, ISO Central Secretariat, Geneva, CH, 2002.

20) I. 6507-1:2018, "Metallic materials — Vickers hardness test.," standard, ISO Central Secretariat, Geneva, CH, 2018.

21) A. E384-11, "Standard test method for Knoop and Vickers hardness of materials.," standard, ASTM International, West Conshohocken, PA, 2011.

22) R. Hill, E. H. Lee, and S. Tupper, "The theory of wedge indentation of ductile materials," *Proceedings of the Royal Society of London. Series A. Mathematical and Physical Sciences*, vol. 188, no. 1013, pp. 273–289, 1947.

23) D. Tabor, *The hardness of metals*. Oxford university press, 1951.

24) G. Pharr, W. Oliver, and F. Brotzen, "On the generality of the relationship among contact stiffness, contact area, and elastic modulus during indentation," *Journal of materials research*, vol. 7, no. 3, pp. 613–617, 1992.

25) W. C. Oliver and G. M. Pharr, "Measurement of hardness and elastic modulus by instrumented indentation: Advances in understanding and refinements to methodology," *Journal of materials research*, vol. 19, no. 1, pp. 3–20, 2004.

26) H. Hertz, "On the contact of elastic solids," *Z. Reine Angew. Mathematik*, vol. 92, pp. 156–171, 1881.

27) A. Bolshakov and G. Pharr, "Influences of pileup on the measurement of mechanical properties by load and depth sensing indentation techniques," *Journal of materials research*, vol. 13, no. 4, pp. 1049–1058, 1998.

28) B. Taljat and G. M. Pharr, "Development of pile-up during spherical indentation of elastic–plastic solids," *International journal of solids and structures*, vol. 41, no. 14, pp. 3891–3904, 2004.

29) Y.-T. Cheng and C.-M. Cheng, "Can stress–strain relationships be obtained from indentation curves using conical and pyramidal indenters?," *Journal of Materials Research*, vol. 14, no. 9, pp. 3493–3496, 1999.

30) K. Tho, S. Swaddiwudhipong, Z. Liu, K. Zeng, and J. Hua, "Uniqueness of reverse analysis from conical indentation tests," *Journal of materials research*, vol. 19, no. 8, pp. 2498–2502, 2004.

31) J. Alkorta, J. Martinez-Esnaola, and J. S. Gil, "Absence of one-to-one correspondence between elastoplastic properties and sharp-indentation load–penetration data," *Journal of materials research*, vol. 20, no. 2, pp. 432–437, 2005.

32) M. Futakawa, T. Wakui, Y. Tanabe, and I. Ioka, "Identification of the constitutive equation by the indentation technique using plural indenters with different apex angles," *Journal of Materials Research*, vol. 16, no. 8, pp. 2283–2292, 2001.

33) J.-L. Bucaille, S. Stauss, E. Felder, and J. Michler, "Determination of plastic properties of metals by instrumented indentation using different sharp indenters," *Acta materialia*, vol. 51, no. 6, pp. 1663–1678, 2003.

34) N. Chollacoop, M. Dao, and S. Suresh, "Depth-sensing instrumented indentation with dual sharp indenters," *Acta materialia*, vol. 51, no. 13, pp. 3713–3729, 2003.

35) X. Chen, N. Ogasawara, M. Zhao, and N. Chiba, "On the uniqueness of measuring elastoplastic properties from indentation: the indistinguishable mystical materials," *Journal of the Mechanics and Physics of Solids*, vol. 55, no. 8, pp. 1618–1660, 2007.

36) A. Atkins and D. Tabor, "Plastic indentation in metals with cones," *Journal of the Mechanics and Physics of Solids*, vol. 13, no. 3, pp. 149–164, 1965.

37) B. Taljat, T. Zacharia, and F. Kosel, "New analytical procedure to determine stress-strain curve from spherical indentation data," *International Journal of Solids and Structures*, vol. 35, no. 33, pp. 4411–4426, 1998.

38) J.-H. Ahn and D. Kwon, "Derivation of plastic stress–strain relationship from ball indentations: Examination of strain definition and pileup effect," *Journal of Materials Research*, vol. 16, no. 11, pp. 3170–3178, 2001.

39) J. Swadener, B. Taljat, and G. Pharr, "Measurement of residual stress by load and depth sensing indentation with spherical indenters," *Journal of Materials Research*, vol. 16, no. 7, pp. 2091–2102, 2001.

40) K. Li, V. Injeti, R. Misra, Z. Cai, and H. Ding, "On the strain rate sensitivity of aluminum-containing transformation-induced plasticity steels: Interplay between trip and twip effects," *Materials Science and Engineering: A*, vol. 711, pp. 515–523, 2018.

41) T. Man, T. Ohmura, and Y. Tomota, "Mechanical behavior of individual retained austenite grains in high carbon quenched-tempered steel," *ISIJ International*, vol. 59, no. 3, pp. 559–566, 2019.

42) T. Man, T. Ohmura, and Y. Tomota, "The effect of boundary or interface on stress-induced martensitic transformation in a fe-ni alloy," *Materials Today Communications*, vol. 23, p. 100896, 2020.

43) T. Suzuki and T. Ohmura, "Ultra-microindentation of silicon at elevated temperatures," *Philosophical Magazine A*, vol. 74, no. 5, pp. 1073–1084, 1996.

44) J. Ruzic, I. Watanabe, K. Goto, and T. Ohmura, "Nano-indentation measurement for heat resistant alloys at elevated temperatures in inert atmosphere," *Materials transactions*, vol. 60, no. 8, pp. 1411–1415, 2019.

45) R. Von Mises, "Mechanics of solids in the plastically deformable state," *NASA, Technical Memorandum*, vol. 88488, p. 1986, 1913.

46) G. C. Nayak and O. C. Zienkiewicz, "Convenient form of stress invariants for plasticity," *Journal of the Structural Division*, vol. 98, no. 4, pp. 949–954, 1972.

47) G. E. Dieter and D. J. Bacon, *Mechanical metallurgy*, vol. 3. McGraw-hill New York, 1976.

48) Y. Liu, S. Varghese, J. Ma, M. Yoshino, H. Lu, and R. Komanduri, "Orientation effects in nanoindentation of single crystal copper," *International Journal of Plasticity*, vol. 24, no. 11, pp. 1990–2015, 2008.

49) M. Liu, C. Lu, K. A. Tieu, C.-T. Peng, and C. Kong, "A combined experimental-numerical approach for determining mechanical properties of aluminum subjects to nanoindentation," *Scientific reports*, vol. 5, no. 1, pp. 1–16, 2015.

50) B. Yang and H. Vehoff, "Dependence of nanohardness upon indentation size and grain size–a local examination of the interaction between dislocations and grain boundaries," *Acta materialia*, vol. 55, no. 3, pp. 849–856, 2007.

51) D. Dugdale, "Cone indentation experiments," *Journal of the Mechanics and Physics of Solids*, vol. 2, no. 4, pp. 265–277, 1954.

52) L. Min, C. Wei-Min, L. Nai-Gang, and W. Ling-Dong, "A numerical study of indentation using indenters of different geometry," *Journal of Materials Research*, vol. 19, no. 1, pp. 73–78, 2004.

53) S. Shim, W. C. Oliver, and G. M. Pharr, "A comparison of 3d finite element simulations for berkovich and conical indentation of fused silica," *International Journal of Surface Science and Engineering*, vol. 1, no. 2-3, pp. 259–273, 2007.

54) M. Kim, J. H. Lee, F. Rickhey, and H. Lee, "A dual triangular pyramidal indentation technique for material property evaluation," *Journal of Materials Research*, vol. 30, no. 8, pp. 1098–1109, 2015.

55) S. D. Mesarovic and N. A. Fleck, "Spherical indentation of elastic–plastic solids," *Proceedings of the Royal Society of London. Series A: Mathematical, Physical and Engineering Sciences*, vol. 455, no. 1987, pp. 2707–2728, 1999.

56) L. Wang and S. Rokhlin, "Universal scaling functions for continuous stiffness nanoindentation with sharp indenters," *International Journal of Solids and Structures*, vol. 42, no. 13, pp. 3807–3832, 2005.

57) M. Chinmulgund, R. B. Inturi, and J. A. Barnard, "Effect of ar gas pressure on growth, structure, and mechanical properties of sputtered ti, al, tial, and ti3al films," *Thin solid films*, vol. 270, no. 1-2, pp. 260–263, 1995.

58) Y.-T. Cheng and C.-M. Cheng, "Scaling, dimensional analysis, and indentation measurements," *Materials Science and Engineering: R: Reports*, vol. 44, no. 4-5, pp. 91–149, 2004.

59) N. Ogasawara, N. Chiba, and X. Chen, "Measuring the plastic properties of bulk materials by single indentation test," *Scripta Materialia*, vol. 54, no. 1, pp. 65–70, 2006.

60) P. S. Phani and W. Oliver, "A critical assessment of the effect of indentation spacing on the measurement of hardness and modulus using instrumented indentation testing," *Materials & Design*, vol. 164, p. 107563, 2019.

61) D. W. Marquardt, "An algorithm for least-squares estimation of nonlinear parameters," *Journal of the society for Industrial and Applied Mathematics*, vol. 11, no. 2, pp. 431–441, 1963.

62) A. Yonezu, T. Ogawa, and M. Takemoto, "Evaluations of elasto-plastic properties and fracture strength using indentation technique," in *Key Engineering Materials*, vol. 353, pp. 2223–2226, Trans Tech Publ, 2007.

63) T.-T. Chen, I. Watanabe, D. Liu, and K. Goto, "Data-driven estimation of plastic properties of alloys using neighboring indentation test," *Science and Technology of Advanced Materials: Methods*, vol. 1, no. 1, pp. 143–151, 2021.

64) Y. Duan, J. Xu, J. Chen, C. Yu, J. Chen, and H. Lu, "The effects of heat treatment on the microstructure and cyclic behavior of a7n01-t4 aluminum alloy," *Materials Characterization*, vol. 131, pp. 201–209, 2017.

65) G. Simmons, "Single crystal elastic constants and calculated aggregate properties," tech. rep., Southern Methodist Univ Dallas Tex, 1965.

66) H. Lüthy, R. A. White, and O. D. Sherby, "Grain boundary sliding and deformation mechanism maps," *Materials Science and Engineering*, vol. 39, no. 2, pp. 211–216, 1979.

67) D. E. Cipoletti, A. F. Bower, Y. Qi, and P. E. Krajewski, "The influence of heterogeneity in grain boundary sliding resistance on the constitutive behavior of aa5083 during high-temperature deformation," *Materials Science and Engineering: A*, vol. 504, no. 1-2, pp. 175–182, 2009.

68) K. Goto, I. Watanabe, and T. Ohmura, "Inverse estimation approach for elastoplastic properties using the load-displacement curve and pile-up topography of a single berkovich indentation," *Materials & Design*, vol. 194, p. 108925, 2020.